The Astronomical Journal, 144:142 (25pp), 2012 November doi:10.1088/0004-6256/144/5/142

A *HUBBLE SPACE TELESCOPE* TREASURY STUDY OF STAR-FORMING REGIONS IN THE LOCAL GROUP. II. YOUNG STELLAR POPULATIONS IN M31

Luciana Bianchi[1], Boryana Efremova[2], Paul Hodge[3], and Yongbeom Kang[1,4]
[1] Department of Physics and Astronomy, Johns Hopkins University, Baltimore, MD 21218, USA; bianchi@pha.jhu.edu
[2] Sigma Space Corporation, Lanham, MD, USA
[3] Astronomy Department, University of Washington, Seattle, USA
[4] Department of Astronomy and Space Science, Chungnam National University, Republic of Korea
Received 2012 May 22; accepted 2012 July 5; published 2012 October 11

ABSTRACT

We studied the young stellar populations of 22 star-forming regions in the Andromeda galaxy (M31), with *Hubble Space Telescope* (*HST*) multi-band imaging from far-UV to *I*. The regions were selected from *Galaxy Evolution Explorer* (*GALEX*) wide-field far-UV imaging; they sample different environments and galactocentric distances from 6 to 22 kpc. They were imaged with 30 *HST* fields (360 distinct images, in six bandpasses), with a pixel scale of 0.38 pc projected on the sky, at the distance of M31. This study is part of *HST* treasury survey program HST-GO-11079, which includes star-forming regions in eight Local Group galaxies. We provide a merged catalog of six-band stellar photometry in the 30 M31 fields, containing 118,036 sources brighter than V and $B \sim 23$ mag. Each *HST* field covers about 0.3 kpc^2 in M31, and contains up to ~7000 stars, of which the number varies by a factor of >7 among the target regions; a large fraction of the sample are hot massive stars, due to our choice of filters and exposures. We derived stellar physical parameters and interstellar extinction for individual sources by spectral energy distribution analysis with model-atmosphere colors, and used the results to infer ages, massive stars content, and extinction of the star-forming regions. Reddening is up to $E(B-V) \lesssim 0.6$ mag in some OB associations, and lowest in the outermost regions (average of $\lesssim$0.12 mag in OB184 at 21.9 kpc). We examined the spatial distribution (clustering) of the hot massive stars, and defined OB associations on various spatial scales from compact to wider, more spread out ones. A hierarchical structuring is observed, with small compact groups arranged within large complexes. Their areas vary from less than 10 to 10^5 pc^2, and masses are up to $\approx 10^5\ M_\odot$, in the scales sampled by our analysis. Their cumulative mass distribution follows a power law, at least in part of the sampled regime. Hot-star counts in the young regions compare very well with integrated measurements of UV flux from *GALEX*.

Key words: dust, extinction – galaxies: individual (M31) – galaxies: star clusters: general – galaxies: stellar content – galaxies: structure – stars: early-type

Online-only material: color figures, extended figures, figure set, machine-readable and VO tables

1. INTRODUCTION

Star formation occurs on a variety of scales, from compact star clusters (typical sizes of 2–3 pc) to the classical OB associations (scales of tens to hundreds of parsecs) to the most sparse structures seen in the outermost regions of disk galaxies, at galactocentric distances up to three to four times the size of the optical disk (Thilker et al. 2005, 2007a; Bianchi 2011 and references therein), to the intracluster medium (e.g., Thilker et al. 2009). Detailed studies of young stellar populations at a single, known distance allow us to learn about the star formation process, and coevolution of dust, in a wide range of environments, and ultimately to understand the causality and regulating factors of star formation and galaxy evolution. Galaxies in the Local Group are close enough that *Hubble Space Telescope* (*HST*) imaging, achieving subparsec resolution, resolves most individual stars, and large telescopes in space and from the ground can obtain spectroscopy of the brightest members (e.g., Bianchi et al. 2001a), to study stellar evolution in different conditions.

In addition to the needed spatial resolution, and low background, *HST*'s broad wavelength range with access to UV wavelengths from space enables in particular a better characterization of the youngest, most massive hot stars, the high $T_{\rm eff}$ optical colors alone of which are not sensitive (Bianchi 2007) and which tend to crowd in compact regions (e.g., Hodge et al. 2011; Bianchi et al. 2001b, 2011c, 2012; Bianchi & Efremova 2006). In the Milky Way (MW), the Sun's location in a spiral arm makes it difficult to comprehensively study the massive star content of star-forming regions, which are located in the MW disk, because the high extinction by interstellar dust limits UV observations, which are in turn essential to discern physical parameters of the hottest stars. Therefore, global characteristics of entire young associations, across a wide environmental variety, can be more easily studied in our neighbor galaxies, while detailed modeling of spectral lines (including wind lines for O-type stars), which requires high-resolution, high-quality spectra, is affordable only for the closest stars (MW or Magellanic Clouds (MC), see, e.g., Bianchi & Garcia 2002; Bianchi et al. 2009; Garcia & Bianchi 2004; Walborn et al. 2002; Pellerin et al. 2002).

We selected a comprehensive sample of 67 star-forming regions in eight Local Group galaxies from *Galaxy Evolution Explorer* (*GALEX*)[5] wide-field far-UV imaging, which provides a snapshot of young populations across entire galaxies unconfused by prior star formation history (older populations contribute light at optical and IR wavelengths but are inconspicuous in the far-UV), with great sensitivity to extremely low star

[5] *GALEX*, a NASA Small Explorer, performed wide-field imaging in two UV bands simultaneously: the far-UV (1344–1786 Å, $\lambda_{\rm eff} = 1528$ Å) and the near-UV (1771–2831 Å, $\lambda_{\rm eff} = 2271$ Å); see Bianchi (2009), Bianchi et al. (2011a, 2011b, 2007) for a characterization of the UV sky surveys, Bianchi (2011) for a review of results on nearby galaxies, and Morrissey et al. (2007) for instrument performance.

formation rates (e.g., Kang et al. 2009; Gil de Paz et al. 2007; Thilker et al. 2005, 2007a, 2007b; Bianchi et al. 2005; Bianchi 2011 and references therein; Calzetti et al. 2005; Marino et al. 2011). In *HST*'s treasury program GO-11079 we imaged the 67 star-forming regions, with six filters from far-UV to *I*, for a total of 882 *HST* images, with the Wide Field and Planetary Camera 2 (WFPC2). In a previous paper (Bianchi et al. 2012) we described the data and results for six dwarf galaxies, which represent the smallest building blocks in the hierarchical galaxy formation scenario, and usually have episodical star formation and low metallicity (e.g., Tolstoy et al. 2009 and references therein). In this paper we study 22 star-forming sites in the Andromeda galaxy (M31), the largest massive spiral besides the MW in the Local Group: its mass was estimated between a few 10^{11} and $2 \times 10^{12}\,M_{\odot}$ by Coté et al. (2000); Corbelli et al. (2010) estimated a total mass of $1.3 \times 10^{12}\,M_{\odot}$ with a 12% baryonic fraction, from a ΛCDM dark-matter halo model fit to the H I rotation curve.

The young stellar populations in the optical disk of M31 have been studied previously with ground-based photometric surveys (e.g., Magnier et al. 1993; Massey et al. 2006, hereafter LGGS; Bianchi et al. 2001b) including studies of variables (e.g., Mould et al. 2004). OB associations have first been defined by van den Bergh (1964); several studies of stellar populations followed (see Hodge 1992 and references therein) up to the recent ground-based surveys mentioned above. Such ground-based surveys have the advantage of a large coverage area, and were used, e.g., by Kang et al. (2009) to select hot stars, define OB associations, and derive the reddening across the disk. However, they suffer from the limitations of (1) resolution (e.g., 1.″5 corresponds to 5.7 pc linear projected scale at M31), which in turn causes two problems: crowded stars are unresolved, and the sky subtraction may have large uncertainties, and (2) optical colors are saturated at the highest $T_{\rm eff}$, as discussed by Bianchi (2007) and later in this paper. Studies were also performed with *HST* (e.g., Rich & Mighell 1995); several works were focused on the bulge and nucleus (e.g., Lauer et al. 2012 and references therein), and much recent work was also devoted to studying the halo and outermost extended populations (e.g., Cuillandre et al. 2001; Chapman et al. 2006; Brown et al. 2009; Tanaka et al. 2010; Bernard et al. 2012; McConnachie et al. 2009). The current and recent star formation was also studied over large galactocentric distances (out to 26 kpc) with *GALEX* UV wide-field imaging (Kang et al. 2009; Thilker et al. 2005) and with IR data (Barmby et al. 2006, 2007); IR data also supported studies of dust (Gordon et al. 2006; Montalto et al. 2009). Our study provides resolved maps of star-forming regions with a physical characterization of single hot stars, and extinction maps with corresponding resolution down to single-star values in the regions, out to a deprojected distance of 22 kpc.

The aim of our treasury program (11079) was to characterize the young populations through the identification and measurement of the hottest, most massive stars. Our study, resolving individual hot stars in several regions, on one hand can be compared with results from wide-field maps to calibrate star formation rate indicators, and in addition can be used to explore the high-mass portion of the mass function (MF), as well as to optimize selection of candidates for follow-up UV and optical spectroscopy, to derive much-needed abundances for young stars, and mass-loss rates. The identification of the hottest stars will also enable interpretation of existing emission-line maps (H_{α}, [O III], and [S II]); see Hodge et al. (2011). Young stellar clusters have also been studied from these data (Hodge et al. 2010, 2011; P. W. Hodge et al. 2012, in preparation) and previous *HST* imaging (e.g., Krienke & Hodge 2007; Barmby & Huchra 2001). A recent compilation of previous M31 cluster data is provided by Kang et al. (2012); the census and

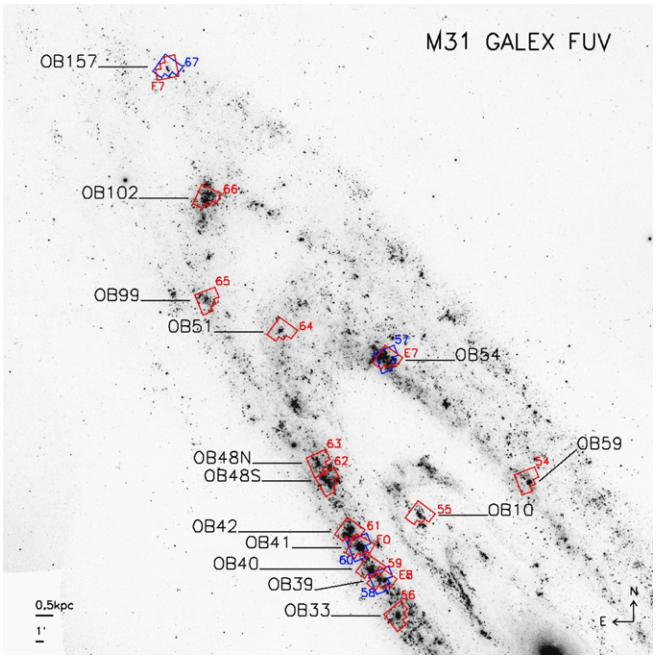

Figure 1. *HST*/WFPC2 footprints overlaid on far-UV *GALEX* imaging (mosaic of several fields): northern disk. Red footprints are complete observations (12 exposures in 6 filters); blue footprints mark fields where some of the exposures failed the first time, and were then repeated. The repeated observations have a different orientation, given that they were obtained at a different time, and no orientation constraints were imposed because the target associations are included in any case (by our choice of centering). The small bar corresponds to 1′.

(A color version of this figure is available in the online journal.)

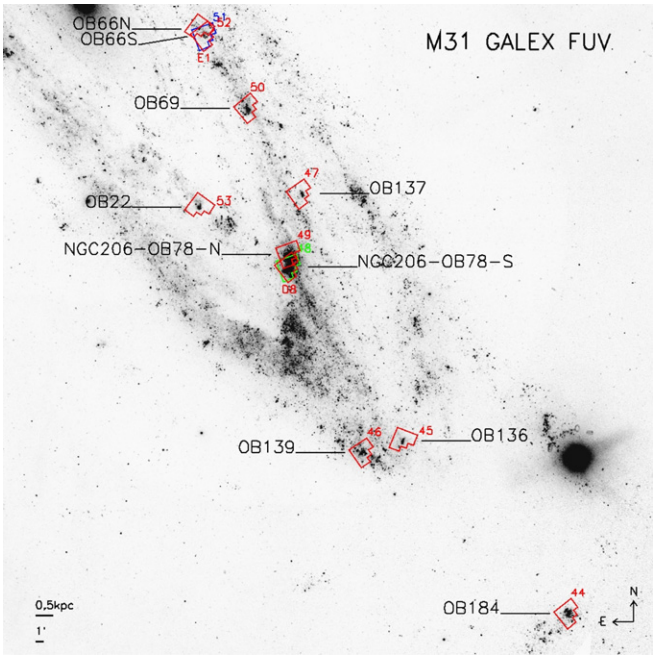

Figure 2. *HST*/WFPC2 footprints overlaid on far-UV *GALEX* imaging: southern portion. Red footprints are complete observations (12 exposures); blue or green footprints are original observations where some of the exposures failed the first time, and were then repeated.

(A color version of this figure is available in the online journal.)

characterization of stellar clusters is now being greatly augmented with the PHAT *HST* survey (Johnson et al. 2012). A census of star-forming regions from UV *GALEX* imaging with low resolution (4.″2, or ∼16 pc) but very deep sensitivity, out to 26 kpc radius, was given by Kang et al. (2009) and used to derive the star formation rate.

In this paper we summarize data characteristics (Section 2) and measurement procedures (Section 3), and present the multiband photometry catalogs (Section 3.2), similar to those for the first six galaxies from Bianchi et al. (2012). We analyze the photometry with stellar models to derive stellar parameters, and interstellar extinction, for individual sources in Section 4; we derive the global properties of the young populations and define OB associations on differing spatial scales in Section 5, and discuss and summarize the results in Section 6.

2. *HST* IMAGING

Twenty-two star-forming regions in M31 were imaged with 30 distinct *HST*/WFPC2 fields between 2007 July and 2008 June as part of treasury program HST-11079. Details of the observations are given in Table 1, and field footprints are shown in Figures 1 and 2, overlaid on a *GALEX* far-UV mosaic of M31. Data were reprocessed by STScI after 2009 August 28 to apply a WF4 pixel-to-pixel bias correction. Our treasury program, for a total of 882 *HST* images, also included several fields in six dwarf galaxies (Bianchi et al. 2012) and M33 (L. Bianchi et al. 2012, in preparation). WFPC2 imaging in six broadband filters (F170W, F255W, F336W, F439W, F555W, and F814W) was acquired at every pointing. The wavelength range including two UV filters shortward of the *U* band facilitates the derivation of stellar temperatures and extinction by interstellar dust, alleviating the $T_{\rm eff}$/extinction degeneracy for hot stars. The filter transmission curves are shown in Figure 3. Details on the observation strategy, data reduction, photometry procedures, and quality assessment tests are given in Bianchi et al. (2012). Here we will only recall the essential information and note what is specifically pertinent to the M31 data sets. Two orbits were spent on each pointing, with exposure times chosen to achieve a uniform depth in all filters for the hot massive stars.

Two exposures were taken with each filter to allow removal of cosmic rays. Coordinates and names of the data sets are given in Table 1. Field names ending with "-COPY" are repeated observations of fields where some of the exposures failed the first time (either they were interrupted, or the stars are trailed, due to guide star reacquisition failures). In all four such cases the entire two-orbit sequence of 12 exposures was repeated; some useful exposures in the first observation provided a repeatability check for the photometry (discussed by Bianchi et al. 2012). The total number of *HST* images amounts to 360 for M31.

Wide-field far-UV *GALEX* imaging, which unambiguously reveals the youngest stellar populations (Figures 1 and 2) was used to choose the *HST* imaging pointings for this program. Each WFPC2 field covers an area of 5.8 arcmin^2, corresponding to ∼0.30 square kpc (projected on the sky) in M31. Contiguous fields, with some overlap, cover the largest star-forming complexes (see Figures 1 and 2 and Table 1).

In Table 1 we also list the deprojected galactocentric distance of each field, obtained using an inclination of $i_{\rm M31} = 77.^\circ7$ (van den Bergh 2000), a position angle of the semi-major axis P.A.$_{\rm M31} = 37.^\circ8$ (de Vaucouleurs 1958), and R.A.$_{\rm M31} = 10.^\circ684583$, Decl.$_{\rm M31} = 41.^\circ267778$ for the galaxy center. We assume a distance of 785 kpc (distance modulus = 24.47; McConnachie et al. 2005).

3. PHOTOMETRY

3.1. Measurement Procedures

In the first paper describing this program (Bianchi et al. 2012) we gave details on the data characteristics, the adopted photometry procedures for the stellar sources, and resulting photometric quality (see also Hodge et al. 2010 for measurements of integrated magnitudes of stellar clusters). We used calibrated science data from the MAST archive, processed for bias removal and flat fielding by the pipeline, we combined images taken with the same filter to mask cosmic rays, and on the combined images we performed source detection and point-spread function (PSF) fitting photometry using the *HSTphot* photometry package (Dolphin 2000). We ran the *hstphot* routine with source-detection independent threshold value of $3.5\,\sigma$, and a total threshold value of $4.0\,\sigma$, which results in a minimum signal-to-noise ratio (S/N) = 4 for the detected sources, and a maximum photometric error of 0.27 mag. The photometry was performed with *HSTphot* option "520," i.e., "refitted sky" for background subtraction, and using default aperture corrections, for a homogeneous processing across the catalog, since aperture corrections determined in individual fields are less accurate in the very crowded regions (see Bianchi et al. 2012 for a discussion and comparison of *HSTphot* options). In the catalog we report the statistical error for each source as determined by *HSTphot*. CTE corrections are a possible additional source of systematic uncertainty, especially in the UV filters. Completeness limits of the photometry were estimated by performing the same photometric procedures on artificially created images. The incompleteness reaches 20% at 21.0, 22.8, 22.9, and 22.0 mag for F336W, F439W, F555W, and F814W, respectively.

Although exposure times, processing, and measurement procedures are identical for the whole program, and the distances of the galaxies comparable, we noticed, when we analyzed the stellar spectral energy distributions (SEDs) with model colors (Section 4), that in a fraction of the M31 stars worse quality for the fits is achieved compared with the samples of the six galaxies published by Bianchi et al. (2012). Excellent fits are obtained in many cases, but for a number of M31 sources UV colors ($m_{\rm F255W}$ and sometimes $m_{\rm F336W}$) are discrepant with optical bands fluxes. We investigated the problem with extensive tests to establish the cause of the occasionally "poor" (or rather, inconsistent) $m_{\rm F255W}$ and $m_{\rm F336W}$ measurements, but no peculiarities were identified in the data, and many tried changes in the procedures, including remeasuring the photometry with different packages, gave no improved results. Finally, we noted that the crowding in some M31 regions (richer in OB stars than several fields studied in the dwarf galaxies) may in some cases limit the photometric quality. Visual inspection of random sources in the fields did not reveal any centering problem. The high overall reddening also causes a lower S/N in the UV filters. In the attempt to characterize the problem, we also compared the *HSTphot* results with IRAF photometry, performed on sources detected from *HSTphot*; we limited the comparison to sources with nominally good photometry (err$_{F555W}$ < 0.05 mag, and $m_{\rm F555W}$ < 20 mag). Both aperture and PSF photometry were compared. Measurements from the two packages in *B*, *V*, and *I* filters compare well within the errors. In the F255W filter significant discrepancies are seen for a number of sources, with the *HSTphot* photometry being either brighter or fainter than IRAF photometry by more than the errors; but measurements are consistent for part of the sources. Less discrepancies are seen in the F336W filter, and in F170W IRAF magnitudes tend to be

Table 1
HST Observations

Visit[a]	Field Name	R.A. (J2000)	Decl. (J2000)	Galactocentric	Exposure Time (s)						R.A. (J2000)	Decl. (J2000)
(field)		(deg)	(deg)	Distance (kpc)	F170W	F255W	F336W	F439W	F555W	F814W	(hrs min sec)	(° ′ ″)
55	M31-OB10	11.044583	41.552833	5.88	600+600	300.0+260.0	300+300	230+260	50+50	60+60	0 44 10.7	41 33 10.2
53	M31-OB22	10.371625	40.851194	7.83	600+600	300.0+260.0	300+300	230+260	50+50	60+60	0 41 29.2	40 51 4.3
49	M31-NGC 206-OB78-N	10.128625	40.754333	9.16	600+600	300.0+260.0	300+300	230+260	50+50	60+60	0 40 30.9	40 45 15.6
D8	M31-NGC 206-OB78-S-COPY	10.128625	40.727556	9.37	600+600	300.0+260.0	300+300	230+260	50+50	60+60	0 40 30.9	40 43 39.2
48	M31-NGC 206-OB78-S	10.128625	40.726833	9.38	0.5+0.5	300.0+260.0	0.5+0.5	230+260	50+50	60+60	0 40 30.9	40 43 36.6
50	M31-OB69	10.237750	41.054278	10.14	600+600	300.0+260.0	300+300	230+260	50+50	60+60	0 40 57.1	41 3 15.4
52	M31-OB66N	10.369542	41.217028	10.37	600+600	300.0+260.0	300+300	230+260	50+50	60+60	0 41 28.7	41 13 1.3
51	M31-OB66S	10.353583	41.201556	10.45	600+600	0.5+0.5	300+300	0.5+0.5	50+50	60+60	0 41 24.9	41 12 5.6
E1	M31-OB66S-COPY	10.353583	41.202250	10.47	600+600	300.0+260.0	300+300	230+260	50+50	60+60	0 41 24.9	41 12 8.1
47	M31-OB137	10.095667	40.878000	10.80	600+600	300.0+260.0	300+300	230+260	50+50	60+60	0 40 23.0	40 52 40.8
E7	M31-OB54-COPY	11.136583	41.871222	11.53	600+600	300.0+260.0	300+300	230+260	50+50	60+60	0 44 32.8	41 52 16.4
57	M31-OB54	11.134792	41.873028	11.62	600+600	0.5+0.5	300+300	0.5+0.5	50+50	60+60	0 44 32.3	41 52 22.9
62	M31-OB48S	11.293542	41.621667	11.92	600+600	300.0+260.0	300+300	230+260	50+50	60+60	0 45 10.4	41 37 18.0
63	M31-OB48N	11.319792	41.658333	11.94	600+600	300.0+260.0	300+300	230+260	50+50	60+60	0 45 16.8	41 39 30.0
64	M31-OB51	11.427500	41.926750	11.97	600+600	300.0+260.0	300+300	230+260	50+50	60+60	0 45 42.6	41 55 36.3
54	M31-OB59	10.748583	41.624361	12.38	600+600	300.0+260.0	300+300	230+260	50+50	60+60	0 42 59.7	41 37 27.7
58	M31-OB39	11.146917	41.419972	12.45	0.5+0.5	0.5+0.5	0.5+0.5	0.5+0.5	50+50	60+60	0 44 35.3	41 25 11.9
60	M31-OB41	11.207292	41.486917	12.57	0.5+0.5	0.5+0.5	0.5+0.5	0.5+0.5	50+50	60+60	0 44 49.8	41 29 12.9
E8	M31-OB39-COPY	11.148750	41.418139	12.58	600+600	300.0+260.0	300+300	230+260	50+50	60+60	0 44 35.7	41 25 5.3
F0	M31-OB41-COPY	11.208750	41.485222	12.67	600+600	300.0+260.0	300+300	230+260	50+50	60+60	0 44 50.1	41 29 6.8
61	M31-OB42	11.237875	41.518139	12.74	600+600	300.0+260.0	300+300	230+260	50+50	60+60	0 44 57.1	41 31 5.3
59	M31-OB40	11.179125	41.442028	12.94	600+600	300.0+260.0	300+300	230+260	50+50	60+60	0 44 43.0	41 26 31.3
56	M31-OB33	11.101083	41.347056	13.20	600+600	300.0+260.0	300+300	230+260	50+50	60+60	0 44 24.3	41 20 49.4
45	M31-OB136	9.8264167	40.369556	15.32	600+600	300.0+260.0	300+300	230+260	50+50	60+60	0 39 18.3	40 22 10.4
65	M31-OB99	11.630625	41.989667	15.50	600+600	300.0+260.0	300+300	230+260	50+50	60+60	0 46 31.4	41 59 22.8
66	M31-OB102	11.638625	42.199194	16.09	600+600	300.0+260.0	300+300	230+260	50+50	60+60	0 46 33.3	42 11 57.1
46	M31-OB139	9.9319167	40.346583	16.36	600+600	300.0+260.0	300+300	230+260	50+50	60+60	0 39 43.7	40 20 47.7
67	M31-OB157	11.752000	42.463722	20.93	0.5+0.5	0.5+0.5	0.5+0.5	0.5+0.5	50+50	60+60	0 47 0.5	42 27 49.4
F7	M31-OB157-COPY	11.756375	42.466556	20.97	600+600	300.0+260.0	300+300	230+260	50+50	60+60	0 47 1.5	42 27 59.6
44	M31-OB184	9.3865417	40.012306	21.90	600+600	300.0+260.0	300+300	230+260	50+50	60+60	0 37 32.8	40 0 44.3

Note. [a] The archive data set names are "U9WQxxyyM" where "xx" is the field/visit (e.g., 48, D8,. . .) and "yy" is the exposure in the sequence of twelve exposures: yy = 01, 02, 03, 04, 05, 06, 07, 08, 09, 0A, 0B, 0C); for example: U9WQ4901M, U9WQ4902M,. . . U9WQ490CM. Data can be downloaded from the MAST archive at http://archive.stsci.edu/hst/search.php. Catalogs and combined images can also be obtained from the author's Web site at http://dolomiti.pha.jhu.edu/LocalGroup.

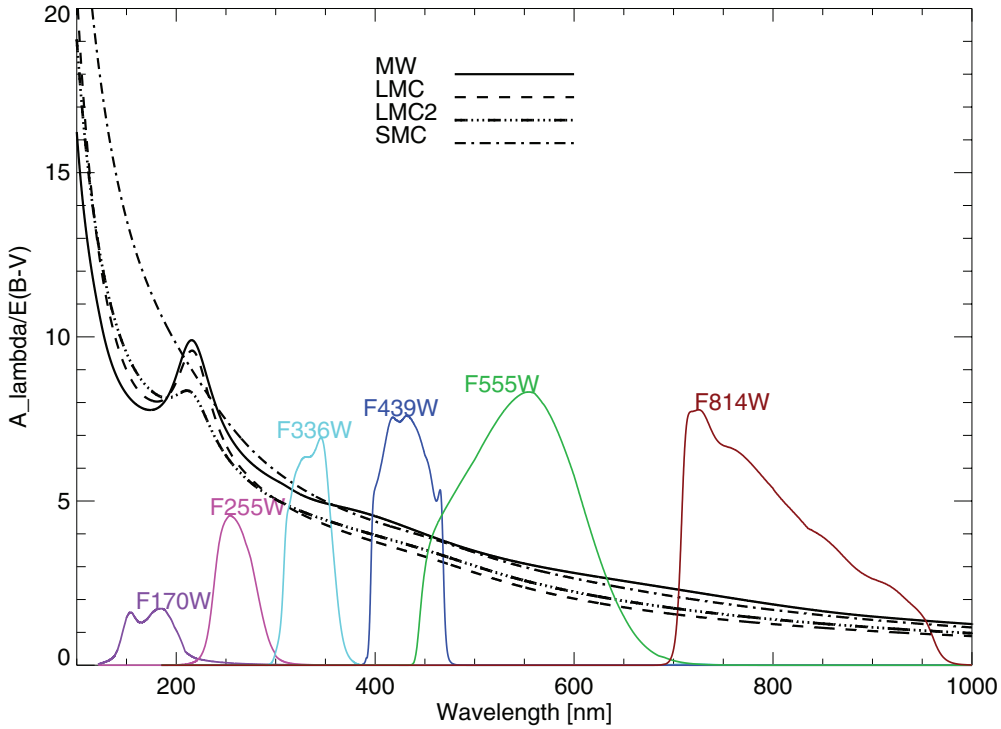

Figure 3. Passbands of the six filters used in this program, shown with some known representative extinction curves $A_\lambda/E(B-V)$, derived for MW and MC sightlines, to illustrate the sensitivity of UV filters to interstellar extinction as well as to stellar $T_{\rm eff}$ for the hottest stars. Broadband colors derived from stellar models, with different extinction effects, are shown as a function of $T_{\rm eff}$ by Bianchi et al. (2012).

systematically brighter. Again, we were not able to detect a trend for the larger errors (or discrepancies) or to associate them with specific causes. In the overlapping fields 48 and D8, F170W magnitudes for stars repeated in different chips show somewhat systematic discrepancies by up to half a magnitude from chip to chip; the consistency is instead nominal (within the errors) in optical bands (Bianchi et al. 2012). We will discuss later how these random errors (exceeding the nominal uncertainty) for a fraction of the sources may affect the analysis (Section 4): the derived $T_{\rm eff}$ seems overestimated for a fraction of sources, indicating that UV bands are inconsistent (too bright) with respect to optical bands. WFPC2 UV filters are also known to be less well calibrated than optical bands (e.g., CTE corrections). A preliminary comparison with hot stars from the PHAT program (L. Bianchi et al. 2012, in preparation) for one field (field 66, included in the currently available PHAT coverage), shows that the photometry is consistent in the *B* band (WFPC2 F439W for this program, ACS F475W for PHAT), while the U measurements are consistent for a fraction of sources but for a subset they are brighter in the WFPC2 F336W measurements from this program than in PHAT WFC3 F336W photometry. Although most of our selected analysis sample has errors in F336W less than 0.1–0.15 mag, 24%/43% of the stars have WFPC2 F336W magnitudes brighter than their ACS counterparts by $\geqslant$0.5/0.3 mag. The filters transmission is comparable: from our model colors, the difference between the WFPC2 and WFC3 "*U*-band" magnitudes is <0.008 mag from $T_{\rm eff} = 6000$ to 50,000 K. A few of the *HST* sources have stars of comparable brightness within half an arcsecond; we excluded these from the comparison. Anomalous dust extinction might also cause a discrepant $m_{\rm F255W}$ in the overall SEDs but this cannot be explored further without spectroscopy; in addition, the random discrepancies between IRAF and *HSTphot* results seen in this filter (and not in *B*, *V*, and *I*) for some of the sources (and not for others) point to a photometry problem, possibly due to source crowding, and to the poorer S/N (and calibration) in the UV filters. The problem does not subsist in the outermost field OB184, suggesting again that crowding may be at least part of the cause.

3.2. The Photometry Catalog

In the merged photometry catalog, published in the online journal and also available, with other supporting data, from the author's Web site,[6] we list all sources detected in either F439W or F555W (the two filters with the deepest exposures) plus one other filter, in order to retain as many true sources as possible. However, such criteria still include a few cosmic rays whose positions accidentally coincide in F439W and F255W, given the very long exposures (and consequent abundance of cosmic rays). Such spurious sources have unrealistic (very blue) colors, which correspond to the difference between the two filters' zero points. They can be eliminated by additionally restricting the sample to sources with significant detection in the F555W filter, which has a rather short exposure. We strongly recommend, for any analysis purpose of stellar sources, to apply such a restriction (F555W magnitude not equal to 99), and furthermore to select only sources with *HSTphot type* = 1 (defined as "good star"), and *sharpness* parameter between −0.3 and +0.3. Such restrictions conservatively eliminate remaining artifacts, which consist mostly of faint sources with unrealistically small errors (see Figure 4 and Figure 2 of Bianchi et al. 2012), although they may also eliminate a few actual stars. We therefore applied the above restrictions to our analysis sample. Figure 4 shows error–magnitude plots for a field as an example. We preferred to publish a very extensive catalog, which contains a small fraction of non-stellar or spurious sources, since it may provide

[6] http://dolomiti.pha.jhu.edu/LocalGroup/

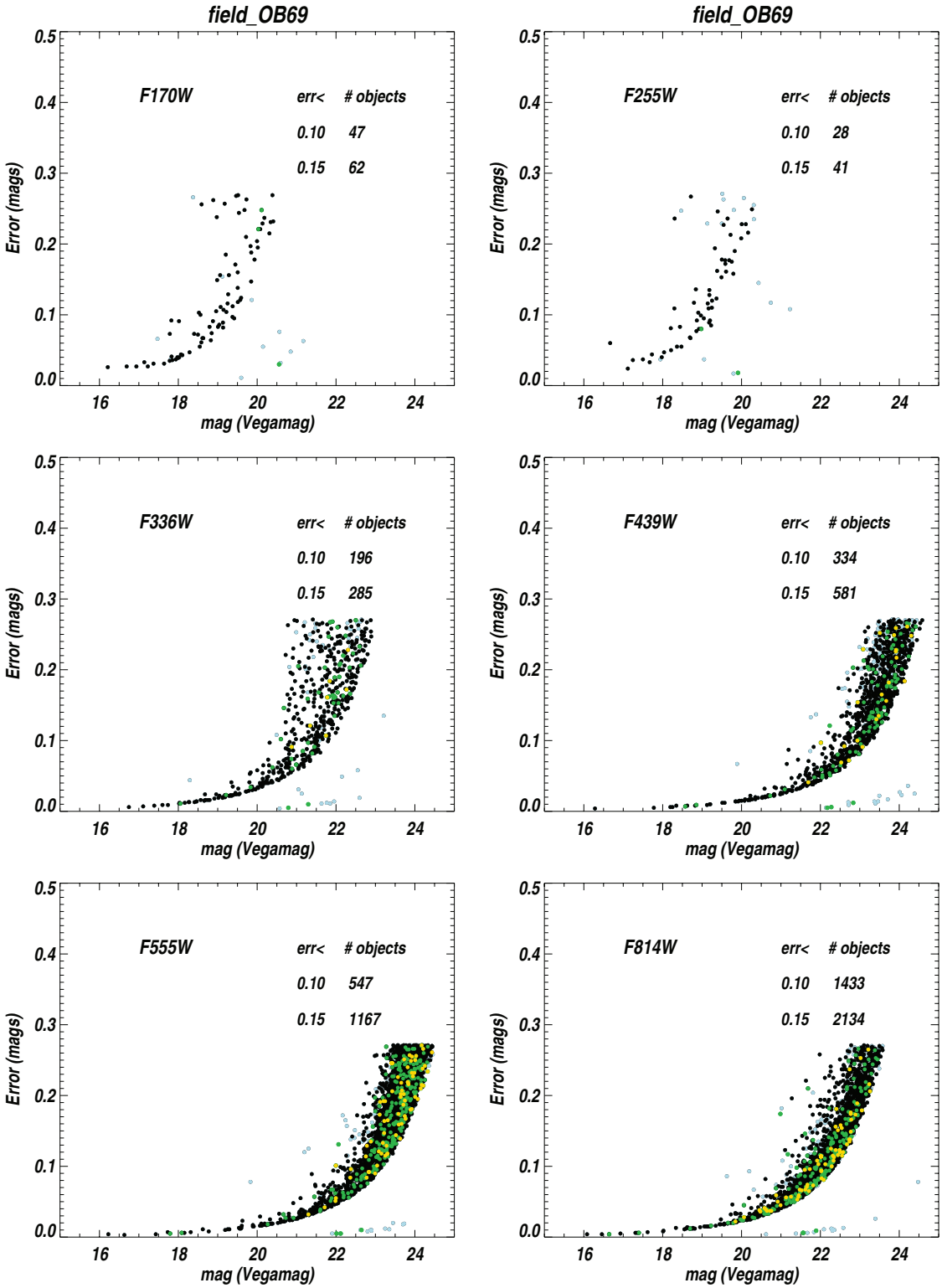

Figure 4. Error–magnitude plots in each filter, for a sample region (OB69). The plots include the two overlapping fields. The yellow dots are sources with *hstphot "Type"* not equal to 1; the green dots have *sharpness* outside our limit of ±0.3; all of these were eliminated in the analysis. The light blue dots are false detections in each filter (probably cosmic rays), which must be eliminated by imposing detection in more than one filter (see text). The 80% completeness limit is ∼21.0, 22.8, 22.9, and 22.0 mag for F336W, F439W, F555W, and F814W, respectively.

(A color version of this figure is available in the online journal.)

identification, at *HST* resolution, of other objects such as X-ray sources, extragalactic background sources, etc., which are not part of our analysis sample.

The number of sources retained in each region with these criteria is given in Table 3. There are several thousand stars in each star-forming region, up to over 12,000 in NGC 206 (covered by two partly overlapping fields), with the exception of two sparse regions, OB157 and OB184 where about 1000 stars are measured (with the restrictive criteria above). These are the two outermost northern and southern fields 67 and 44,

with deprojected galactocentric distances of 20.9 and 21.9 kpc, respectively.

To summarize, in the catalogs available online we retained sources with detection in either F555W or F439W plus one other filter, and any value of *sharpness* and *type* parameters, in favor of completeness (118,036 sources in total, after merging repeated measurements in overlapping fields to generate a unique-source catalog). However, we restrict the analysis sample to sources with detection in F555W plus another filter, *HSTphot type* = 1 and $|sharpness| < 0.3$ (104,774 sources). The photometry catalog given as a VO-formatted online table contains the following columns: (1) running number, (2) region, (3) object ID, following IAU designation, (4–5) R.A. and Decl., (6–17) magnitude (Vega mag) and error, in each filter from F170W to F814W, (18–21) U, B, V, and I magnitudes, transformed from the m_{F336W}, m_{F439W}, m_{F555W}, m_{F814W} magnitudes to the Johnson system with *HSTphot*, (22) sharpness parameter, (23) "type," (24–25) visit/field (see Table 1) and detector (chip). A sample is shown in Table 2. The catalog lists the *HSTphot* nominal errors from the procedure, but as we discussed in the previous section, the actual errors in the UV bands may be several σ in part of the sources.

In the catalog, the magnitudes of objects detected in overlapping images are averages of the individual measurements weighted by their errors. Column 25 records on which detector (chip) the source has been measured, so that it is possible to retrace sources measured on WF4, which has slightly larger systematic errors. Their coordinates refer to one of the images, which is provided in column 24. The astrometry was derived using the *metric/wfpc2* IRAF routine to translate the PC/WF coordinates into right ascension and declination. However, coordinate shifts have been applied to some overlapping fields, in order to merge the photometric measurements. The shifts are listed at the bottom of Table 1. They must be subtracted if finding charts are to be produced from the original images. The WFPC2 coordinates have not been registered to standard frames because we felt it was more important for most uses of these data (small fields, very high resolution) that the catalog photometry can be uniquely associated with an *HST* source in the original image. In matching our *HST* catalogs with other catalogs, we found offsets no larger than $1''$, which is comparable to the resolution of ground-based catalogs, for example, but most bright stars in these catalogs are resolved into multiple components by *HST* imaging (see, e.g., Bianchi et al. 2012 for a discussion), and $<0\farcs5$ with existing PHAT data, although the current overlap is still very small.

4. ANALYSIS AND RESULTS

4.1. Color–Magnitude Diagrams and Color–Color Diagrams

Figure 5 shows observed (not corrected for reddening) color–magnitude diagrams (CMDs) for the 22 regions, in four colors constructed from our set of WFPC2 filters. We marked with vertical lines stellar model colors, computed in the WFPC2 passbands, for $T_{\rm eff}$ = 49,000, 30,000, 20,000, and 15,000 K. Both intrinsic (long lines) and reddened model colors ($E(B-V) = 0.25$, MW-type dust, $R_V = 3.1$; short lines) are shown, for two gravity values, bracketing most expected cases. Colors constructed from different filters illustrate the sensitivity of ultraviolet measurements to discern the hottest stars from intermediate temperature objects. The plots also provide an estimate at a glance of the average reddening of each region from the observed position of the "blue plume." Such a feature is sometimes used to estimate $E(B-V)$ by eye from optical color–magnitude diagrams (e.g., Massey et al. 2006). However, in our case we will use an SED model analysis to derive $E(B-V)$ concurrently with stellar parameters for each source with enough photometric measurements (Section 4), thanks to our multi-band coverage.

Figure 6 shows color–color diagrams with two combinations of WFPC2 filters for each of the 22 regions, and model colors (solar metallicity) of different gravity. Sources with small photometric errors are shown with larger dots in all figures. In the plots including a UV band, fewer detected sources are seen than in the optical bands, since the hot stars are less numerous. In some panels (regions) the data, especially those with good photometry, cluster between model curves with reddening $E(B-V) = 0$ to 0.25 mag (OB78, OB69, OB137, OB99, OB157, OB184). In OB40 and OB41 the hot stars, detected in UV (right panel), are less spread along the reddening lines than the stars measured in optical filters (left panel). Our quantitative analysis (next section) will show that in fact some cooler star samples have higher reddening than the hot-star clusters, possibly indicating that they lay deeper in the disk, and that our choice of the UV-brightest regions tends to select starbursts above the main galaxy disk toward our line of sight rather than behind the disk, not surprisingly. In other regions the majority of data points are between $E(B-V) = 0.25$ and 0.5 mag model lines (e.g., OB54, OB66, OB33), and finally other fields include a wider range of reddening. This will be discussed quantitatively in the analysis of stellar SEDs below. Note that for "field_NGC 206-OB78" we combined two WFPC2 fields (49, 48, and the repeat D8), and for "field_OB66" we combined WFPC2 fields 51 and 52 (with the repeat E1); therefore these two cases enclose almost twice the area as the others.

4.2. Derivation of Physical Parameters for Stellar Sources and Extinction

We derived the stellar parameters, and reddening by interstellar dust, by fitting the multi-band photometry of each source with grids of model colors, computed in the WFPC2 passbands from stellar atmosphere models with a range of $T_{\rm eff}$ and gravity values (and metallicity). Each model spectrum was progressively reddened by increasing $E(B-V)$ values in small steps, before computing the broadband magnitudes, assuming different types of extinction curves $A_\lambda/E(B-V)$. Figures 5–6 show that the inclusion of short-wavelength measurements to the far-UV gives us a greater leverage to discern the hottest stars, compared with optical catalogs (see also Bianchi et al. 2012; Bianchi 2007, 2009). The hottest, brightest stars have measurements in all six filters.

A standard χ^2 minimization technique was used. The original $T_{\rm eff}$ grid (in the range 49,000 K–3500 K, for the higher gravity, $\log g = 5.0$; the $T_{\rm eff}$ range is smaller for lower gravities) is interpolated in subsequent finer steps around the solution found in each iteration, with a number of iterations (up to five), to better define the χ^2 minimum and χ^2 contours from where errors are estimated. See also Bianchi et al. (2012) and references therein for more details. We compared results from models with solar ($z = 0.02$), supersolar ($z = 0.06$), and subsolar ($z = 0.008$) metallicity, and assuming four different selective extinction curves, shown in Figure 3. The main parameters which determine the observed SED are $T_{\rm eff}$ (the major parameter determining the intrinsic colors) and interstellar reddening. Colors at a given temperature also depend on gravity, but only slightly for hot sources and conspicuously below about 10,000 K

Table 2
HST Photometry Catalog

No.	Galaxy	Source IAU Identifier	R.A. (J2000) (degrees)	Decl. (J2000) (degrees)	m_{F170W} (mag)	Err (mag)	m_{F255W} (mag)	Err (mag)	m_{F336W} (mag)	Err (mag)	m_{F439W} (mag)	Err (mag)	m_{F555W} (mag)	Err (mag)	m_{F814W} (mag)	Err (mag)	U (mag)	B (mag)	V (mag)	I (mag)	Sharpness	Type	Frame	Chip
0	M31	J003727.8+400131	9.3661833	40.0253220	99.00	99.00	99.00	99.00	99.00	99.00	99.00	99.00	23.07	0.10	21.41	0.06	99.00	99.00	23.06	21.37	0.033	1	44	1
1	M31	J003727.9+400135	9.3662567	40.0265846	99.00	99.00	99.00	99.00	99.00	99.00	99.00	99.00	23.92	0.21	22.78	0.16	99.00	99.00	23.90	22.74	0.337	1	44	1
...																								
101	M31	J003730.1+400032	9.3758249	40.0090942	19.33	0.18	19.23	0.17	20.21	0.05	21.55	0.04	21.74	0.05	21.75	0.10	20.76	21.57	21.74	21.75	−0.044	1	44	0
102	M31	J003730.2+400030	9.3758831	40.0083733	99.00	99.00	99.00	99.00	99.00	99.00	23.53	0.24	23.63	0.26	99.00	99.00	99.00	23.53	23.63	99.00	0.000	1	44	0
103	M31	J003730.2+400111	9.3759098	40.0198135	19.68	0.13	20.17	0.21	20.91	0.06	22.14	0.06	22.22	0.09	22.01	0.23	21.41	22.16	22.22	22.00	−0.012	1	44	1

Notes. This table is also available at the author's Web site at http://dolomiti.pha.jhu.edu/LocalGroup/. Magnitude values of 99. are assigned to non-detections in a given filter. *HSTphot* parameters "sharpness" and "type" are given in columns 22 and 23: only sources with type = 1 ("good star") and sharpness between −0.3 and 0.3, and detection in the F555W filter, were used in the analysis. Coordinate shifts have been added to fields D8: δR.A. = −0.″00013, δDecl. = −0.″00018; E1: δR.A. = 0.″0001, δDecl. = −0.″00003; E8: δR.A. = −0.″0001, δDecl. = 0.″0002; and F0: δR.A. = 0.″00016, δDecl. = −0.″00017.

(This table is available in its entirety in machine-readable and Virtual Observatory (VO) forms in the online journal. A portion is shown here for guidance regarding its form and content.)

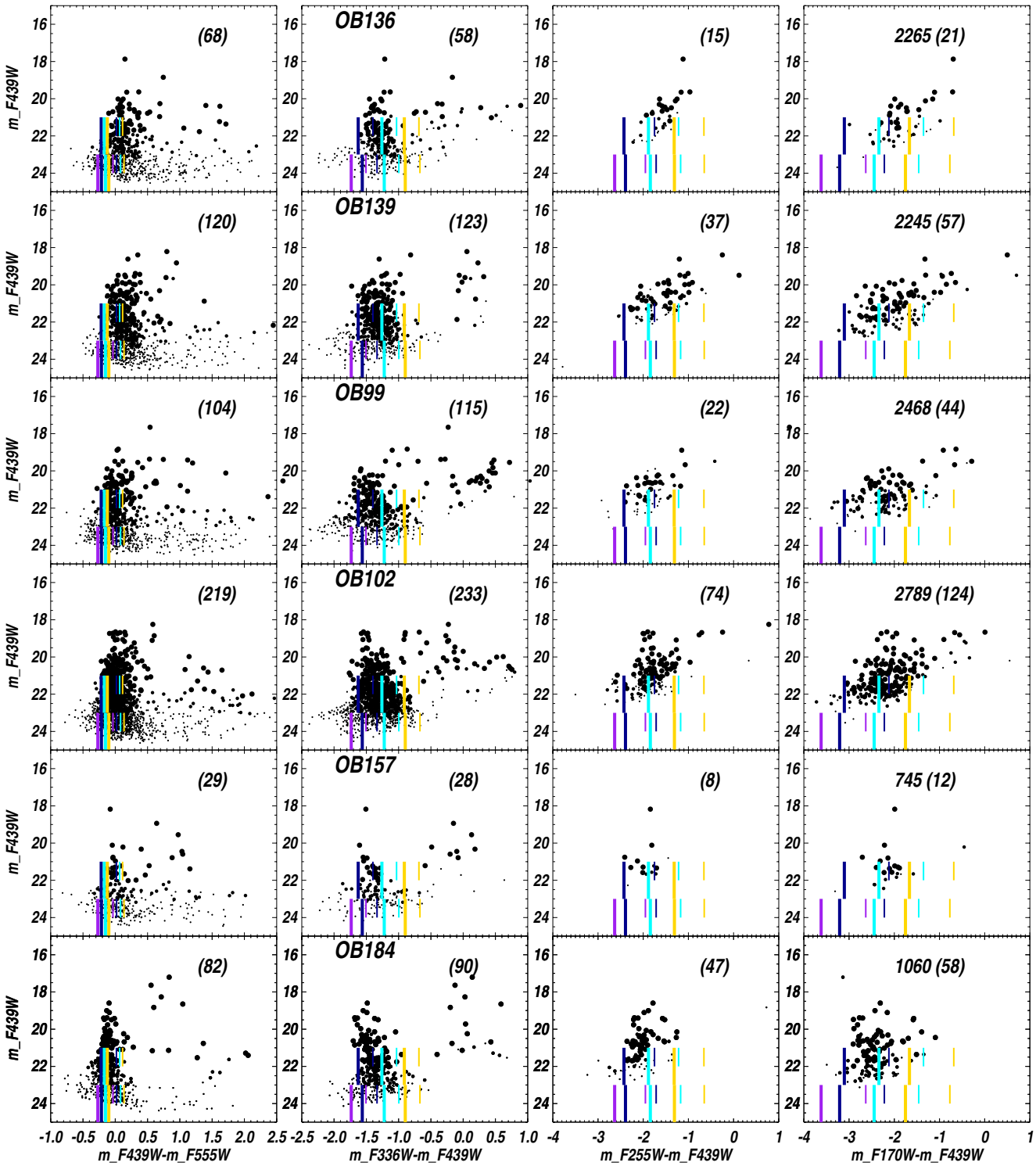

Figure 5. Color–magnitude diagrams for the 22 regions: one region per row, four colors shown. Large dots are sources with photometric errors <0.15 mag in F255W, <0.1 mag in F336W, and <0.05 mag in F439W and F555W. The error cuts are applied only to the filters used in each plot, which explains the different number of large dots in each panel (given in parenthesis). The total number of sources in the analysis sample (as described in Section 3.2) is also reported in each right panel. Vertical lines mark stellar model colors ($z = 0.02$) with $T_{\rm eff} = 49{,}000$, 30,000, 20,000, and 15,000 K (left to right; purple/blue/cyan/yellow in the color version): the long lines mark intrinsic model colors, and short lines (displaced redward) are models reddened with $E(B-V) = 0.25$, assuming MW-type dust. Dust more typical of SF regions would cause higher reddening of colors in the UV filters. The lower set of model color bars is for log $g = 5.0$; the upper set for log $g = 3.5$ and does not include $T_{\rm eff} = 49{,}000$ K. Panels for the other regions are shown in the online journal.

(An extended version of this figure is available in the online journal.)

(see Figure 6). Metallicity also affects the colors, given its influence on line blanketing, but the effect is very subtle for hot stars (Bianchi et al. 2012). The selective extinction curve $A_\lambda/E(B-V)$ depends on the properties of the dust grains (e.g., Mathis 1994), and has been found to vary with environment, especially in locations of intense star formation, the differences being more conspicuous in the slope shortward of ∼1800 Å, and in the strength of the broad absorption feature near 2175 Å

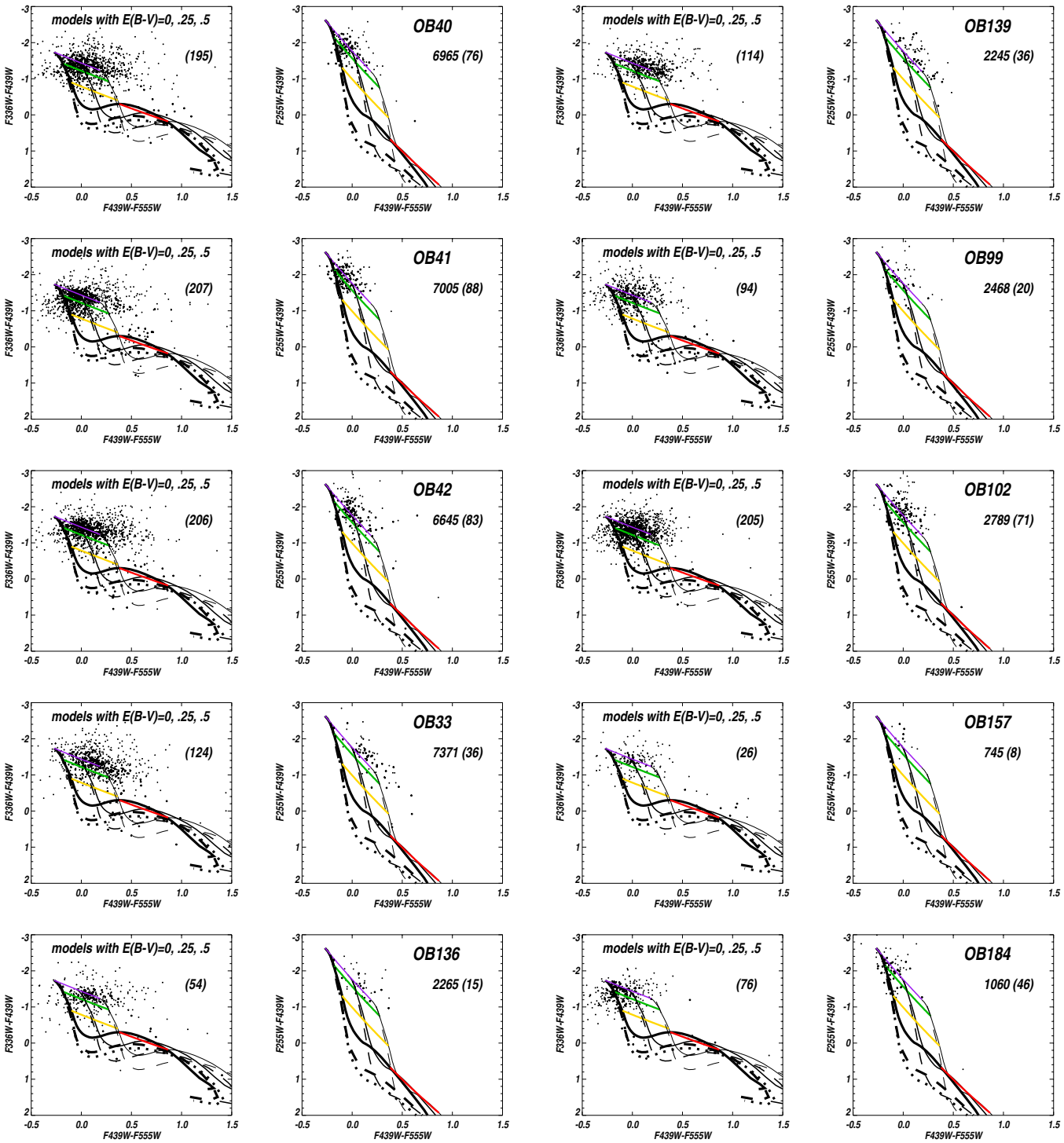

Figure 6. Color–color diagrams. Two are shown for each region: the left plot corresponds to the classical $U - B$, $B - V$ diagram, and the right panel shows a color with a UV filter, which better separates the hottest stars. Large dots are sources with photometric errors <0.15 mag in F255W, <0.1 mag in F336W, and <0.05 in F439W and F555W (error cuts are applied only to the filters used in each plot; the number of sources is given in parenthesis). The total number of sources in the analysis sample (Section 3.2) is also reported in each right panel. Models colors (solid lines for log $g = 5$, dashed for log $g = 3.5$ and dotted for log $g = 3.0$) for solar metallicity are shown with reddening of $E(B - V) = 0$, 0.25 and 0.50 mag (thick, medium, and thin lines). Colored lines also connect reddened and unreddened models at $T_{\rm eff} = 49$ kK, 25 kK, 15 kK, and 7 kK (purple to red) indicating the reddening vectors. Panels for the other regions are shown in the online journal.

(An extended, color version of this figure is available in the online journal.)

(known as the "bump"). Curves of $A_\lambda/E(B - V)$ from UV spectroscopy of hot stars have been derived in a few sightlines in the Milky Way, Magellanic Clouds, M31 and M33 (e.g., Misselt et al. 1999; Gordon & Clayton 1998; Bianchi et al. 1996, 2004 and references therein), and a few are shown in Figure 3.

Deriving the actual $A_\lambda/E(B - V)$ curve in each sightline requires UV spectroscopy, which can only be afforded for a few stars. In order to estimate physical parameters from photometry, we repeated the analysis assuming different known extinction curves (such as those plotted in Figure 3) and gauged the effects

that such choices have on the results from SED fitting. In some favorable cases one could determine the most plausible assumption, if one extinction curve gives a significantly better fitting than others; however, the matter is complicated by some degeneracy with $T_{\rm eff}$, and by the influence of gravity and metallicity (see also Bianchi et al. 2012). In all cases we can at least estimate the uncertainty that the lack of information on the extinction curve carries on the resulting stellar parameters and $E(B-V)$. In the following discussion, we will indicate with "$R_V = 3.1$" results obtained from model grids reddened assuming the MW typical curve with $R_V = 3.1$, taken from Cardelli et al. (1989); "LMC2" indicates that we used the curve derived from Misselt et al. (1999) in this LMC region; "avgLMC" will label results obtained assuming the extinction curve derived in LMC sightlines by Gordon & Clayton (1998); and "SMC" indicates the very steep curve derived along SMC sightlines by the same authors.

In Table 4 we provide coefficients for reddening correction in each broadband filter used in this program, for the benefit of potential users of our catalog (or any catalog in these filters), derived for the four extinction curves cited above. They are computed comparing magnitudes of models reddened with a differential extinction of $E(B-V) = 0.4$ mag, and averaging across the $T_{\rm eff}$ range 30,000–12,500 K. This is more accurate than computing $A_\lambda/E(B-V)$ at the $\lambda_{\rm eff}$ of the passband, especially when the spectral slope across the passband is steep. Figure 3 shows that our filters' combination is little affected by the strength of the 2175 Å bump (the F255W and F170W passbands being on the sides of it), but the UV slope of the $A_\lambda/E(B-V)$ curve can strongly influence the F170W and F255W measurements. Table 4 quantifies the effect. The extinction curve is found to be UV-steep only in extremely intensive star formation sites at low metallicity, such as the SMC, some sites in NGC 6822 (e.g., Efremova et al. 2011) or starburst galaxies (e.g., Calzetti et al. 2005, 1995). Using *HST*-UV spectra of a few bright stars, Bianchi et al. (1996) had explored $A_\lambda/E(B-V)$ in a few M31 sightlines and found it to have a UV slope similar to the Milky Way $R_V = 3.1$ curve, but possibly a weaker bump. These few measurements cannot be taken as representative of a whole galaxy, but for the time being there is no other spectroscopic information. Therefore, we assumed first a Milky Way extinction curve with $R_V = 3.1$, and explored the effect of metallicity in Figure 7. The most evident effect is that the SED-fitting solution is quite stable (or insensitive to metallicity) in most cases. A comparison as in Figure 7 adopting a steep UV extinction curve $A_\lambda/E(B-V)$ (e.g., "LMC2") similarly indicates supersolar metallicity to be slightly better in many cases, but produces more scatter in OB40 and an opposite trend (solar metallicity preferable) in OB137 and OB136.

Dust properties, and metallicity, can be expected to largely vary across the entire galaxy and even within each field, the UV extinction curves being extreme in regions of intense star formation, and younger stars (or stars in regions of prolonged intense star formation) having possibly higher metallicity than older stars. Finer constraints on these parameters require follow-up spectroscopy. For this reason, we examined results from our SED analysis obtained under a range of assumptions, the most appropriate combination likely being different case by case.

Finally, we shall mention two sources of uncertainty in the SED-fitting results, which may be not accounted for in the formal errors derived from χ^2 contours. First, as recalled by

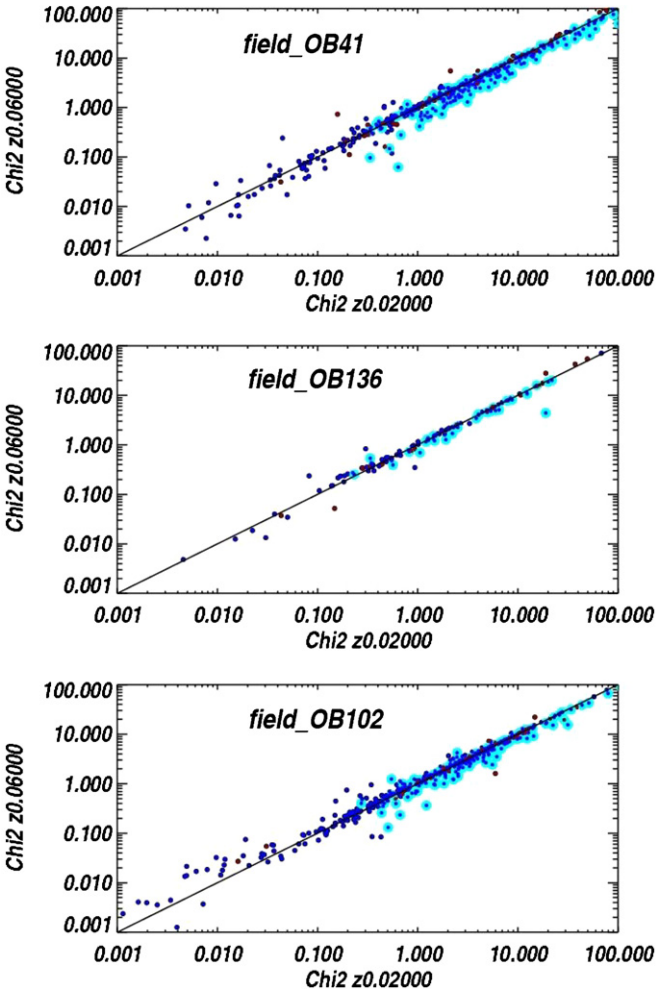

Figure 7. Comparison of χ^2 from SED fitting using models with solar metallicity (x-axis) or supersolar metallicity (y-axis, $z = 0.06$). Milky-Way-type extinction with $R_V = 3.1$ was assumed in the case shown. Cyan circles mark sources with good photometry measured in all six filters; blue/red dots indicate stars with $T_{\rm eff}$ higher/lower than 17,000 K (as derived from SED fitting). Supersolar metallicity gives a better fit (a lower χ^2) in some cases. Three fields are shown as an example of the sensitivity of the photometric analysis to these parameters.

Bianchi et al. (2012), uncertainties are larger for the hottest stars than for intermediate temperature ones. Then, as explained in Section 3, we suspect that a fraction of our sources may have worse photometry than the formal errors indicate, in the UV filters. The problem is notable for crowded fields, and not in the sparse OB184, for example. When we examine the SED-fitting results, we find that a fraction of sources has $T_{\rm eff}$ equal to the maximum value of the grid (49,000 K): this may be true in a few cases, but it often means that the χ^2 procedure runs to one extreme of the model colors range without finding a good physical solution. This fraction is between 15% and 20% of the hot stars for several fields (but less than 5% for OB184). More specifically, histograms of the derived $T_{\rm eff}$ in each field show the sources to be variously distributed above 20,000 K, more or less as expected considering the stellar initial mass function (IMF) and our photometry selection, except for a sharp peak at the maximum $T_{\rm eff}$ value of the grid, indicating that problems with the photometry, or the model grid, or both, prevented a meaningful solution for stars in that peak. We looked at the individual SED for these sources and the derived parameters, and found the majority to have a radius too small for a very

hot main sequence star when the best-fit model is scaled to the m_{F555W} magnitude: in sum, either UV magnitudes are too bright, or optical magnitudes are too faint, or/and our model grids do not have blue-enough colors. Our model grids do not include WR-type spectra for example; these can be hotter and less visually luminous than models appropriate for main sequence and supergiants, and might fit better some of the "suspicious" SEDs; however, the high number of such cases would still be unrealistic. If the photometry issue relates to crowding, this should be worse in V and I bands, since UV-emitting stars are rare, and a background overcorrection may lead to fainter optical magnitudes. Because our experiments with different photometry procedures indicated the UV magnitudes to be less stable, and possibly the zero points are less accurate, as a further test we performed SED-fitting by giving less weight to the UV bands; the results were slightly worse rather than improving, since we also lose sensitivity to the hot temperatures.

We have attempted to isolate such cases (sources with T_{eff} apparently too hot, radius too small). Because an overestimate of T_{eff} usually corresponds also to an overestimate of $E(B-V)$, we first checked whether the high average values of reddening derived for the regions may be caused by these badly fitted sources. The derived $E(B-V)$ from them is quite widely distributed, similarly to the histogram of $E(B-V)$ values found for the rest of the sources, indicating that the probable error (overestimate) on T_{eff} does not propagate significantly on the reddening. In Section 5 we give number counts for hot massive stars in each field, and average reddening derived from them; to quantify the possible problems induced by the suspicious sources we also give resulting values after excluding these cases (third and fourth rows for each field in Table 3). Again, this shows a little influence on the average reddening values.

For a validation of our photometric estimates, we searched the literature for stars with previous spectroscopic classification. Optical spectra for M31 hot stars were published by Cordiner et al. (2011), Massey et al. 2006, Trundle et al. (2002); Bresolin et al. (2002) obtained UV spectra for five early-B stars. A few earlier works are basically included in these samples, which provide refined classification in some cases. Targets for spectroscopy are of course chosen among the brightest stars, and unfortunately most of the objects from these works that are included in the footprint of our fields turn out to be multiple sources at the *HST* resolution. Source LGGS_J004030.52+404529.0 from Massey et al. (2006), classified as "Blue SG, B5I," is actually a cluster (No. 5 of Barmby & Huchra 2001), resolved into many stars in our *HST* catalog. For a few stars we have a bona-fide identification: the ground-based magnitudes reasonably match *HST* optical magnitudes, and there are no multiple matches of comparable brightness within 1 arcsec (which would be unresolved in the ground-based data and cause a composite spectrum to be observed). Out of these matched stars (1 from Trundle et al. 2002: OB10-64, 17 from Cordiner et al. 2011, and 10 from Massey et al. 2006, with 5 stars in common), most hot stars (earlier than B2) have photometrically derived T_{eff} appropriate for the spectral types, and about 8 later type stars have overestimated T_{eff}, some cases by up to ~6000 K. We examined the SEDs of these cases and they are among those with bad U-band photometry discussed earlier; most of the matched stars (20) are in OB78, where the UV photometry is worse, as discussed above. In sum, we can conservatively estimate that for up to 30% of the stars T_{eff} could be overestimated, and the UV to U photometry unreliable. Further spectroscopy of isolated targets selected from this program in other regions would be crucial for a meaningful assessment.

4.3. H-R Diagrams

We constructed H-R diagrams (HRDs) for each star-forming region, dereddening the photometry with the $E(B-V)$ values derived in Section 4.2, and scaling it for the distance to M31. Derivation of two free parameters (T_{eff} and $E(B-V)$) by χ^2 fitting requires at least four independent measurements; therefore it was possible only for a subset of the stars (Table 3, columns 6 and 7). For stars with measurements in fewer filters we adopted average $E(B-V)$ values for the region, derived from the subsample with SED-fitting results, and also provided in Table 3. Figure 8 (partly published only in the online journal) shows an absolute-mag–dereddened-color diagram for each region, in F439W-F555W, F439W. Isochrones for log(ages) of 6.6, 7.0, 7.5, 8.0, 8.5 (years) are overplotted from Padua models (Marigo et al. 2008; Girardi et al. 2010) for solar metallicity. Initial-mass values of 5, 9, 15, 20, 40, and 60 $M_\odot$ are marked along each isochrone with diamonds of increasing size. In each diagram we plot all the stars measured in the *HST* field(s), not just the stars in the targeted OB association of that field, since associations can be, and have been, defined in various ways, historically and from the present data, as will be discussed in the next section. Stars along the 4 Myr isochrone are seen in all regions, even the outermost ones, and often on 10 and 30 Myr isochrones as well.

5. DISCUSSION. GLOBAL PROPERTIES OF THE YOUNG POPULATIONS

5.1. The Massive Star Content

Using the reddening values derived in the previous section, we counted the stars bluer than −0.05 mag in $(m_{F439W} - m_{F555W})_0$, and brighter than $M_{F555W} < -4.36$ and −2.04 mag: these absolute magnitudes correspond, on a 4 Myr isochrone, to initial masses of 20 and 9 $M_\odot$. However, on a 10 Myr isochrone, stars with these initial masses would have $M_{F555W} = -7.25$ and $-2.25\,M_\odot$, and our M_{F555W} limits above would then include less massive stars, which are more numerous. Therefore, counting stars more massive than a given limit (of initial mass) is more uncertain when isochrones of similar ages are well populated, because it is hard to distinguish populations differing by a few Myr of age (<10 Myr) by their dereddened color. The photometric errors make the width of the observed main sequence comparable to the separation between a few Myr and 10 Myr isochrones, except for the highest masses (Figure 8). Of course this is true for all such studies. The intrinsic colors, according to the evolutionary isochrones, are $M_{F439W} - M_{F555W} = -0.26$ mag (20 $M_\odot$) and $M_{F439W} - M_{F555W} = -0.223$ mag (9 $M_\odot$) at 4 Myr, and $M_{F439W} - M_{F555W} = -0.096$ mag (20 $M_\odot$) and $M_{F439W} - M_{F555W} = -0.221$ mag (9 $M_\odot$) at 10 Myr. Magnitudes and colors for a star with initial mass of 9 $M_\odot$ are less different, within this age range, than those for higher masses, therefore the counts in columns 13 and 14 of Table 3 give a good indication of the number of stars more massive than 9 $M_\odot$, while the counts for the more massive stars (column 12) may be overestimated if an age spread is present. The star counts given in columns 12–15 of Table 3 are obtained including all stars bluer than $(m_{F439W} - m_{F555W})_0 < -0.05$ mag; this color cut is redder than the theoretical colors by about 0.2 mag, to take into account the observational width of the "blue plume" (a combination of photometric errors and

Table 3
Results from *HST* Photometry

Region	Fields	Area[a]	Galactocentric	Sources		Stars with		$E(B-V)$ from SED Model Fitting[e]			Hot Stars with[f]			Hot Stars with[g]			
	(visits)	(kpc^2)	Distance	Total[b]	Analysis[c]	Fitted SED[d]		Hot Stars	All Stars	Cool Stars	$(M_{F439W}-M_{F555W})_o < -0.05$ mag			$T_{\rm eff} > 18$kK and $M_{F555W} <$			
			(kpc)	Sample	Sample	Tot.	$T_{\rm eff} > 18$kK	Median/Mean	Median/Mmean	Median/Mean	$M_{F555W} < -4.36$	< -2.04	< -2.254	< -4.05	< -3.25	< -2.50	< -1.65
OB10	55	0.30	5.88	7835	6839	347	328	$0.30/0.31 \pm 0.18$	$0.29/0.30 \pm 0.19$	$0.14/0.25 \pm 0.28$	32^{+0}_{0}	244^{+1965}_{-36}	197^{+943}_{-11}	77	136	214	285
				195	188	**181**	**175**	$\mathbf{0.28/0.30 \pm 0.17}$	$\mathbf{0.28/0.30 \pm 0.17}$	$\mathbf{0.49/0.36 \pm 0.31}$	$\mathbf{32^{+0}_{-1}}$	$\mathbf{146^{+0}_{-1}}$	$\mathbf{146^{+0}_{-2}}$	**70**	**110**	**148**	**171**
						347	231	$0.27/0.29 \pm 0.19$	$0.29/0.30 \pm 0.19$	$0.14/0.25 \pm 0.28$	27^{+1}_{-1}	201^{+1170}_{-16}	177^{+471}_{-14}	58	103	153	195
						181	150	$0.28/0.29 \pm 0.17$	$0.28/0.30 \pm 0.17$	$0.49/0.36 \pm 0.31$	27^{+0}_{-1}	145^{+0}_{-1}	143^{+2}_{-5}	57	103	146	171
OB22	53	0.30	7.83	5115	4609	349	300	$0.33/0.34 \pm 0.17$	$0.33/0.34 \pm 0.17$	$0.29/0.31 \pm 0.20$	19^{+1}_{-2}	331^{+2009}_{-54}	269^{+1139}_{-36}	48	105	200	273
				175	171	**168**	**142**	$\mathbf{0.33/0.35 \pm 0.14}$	$\mathbf{0.33/0.34 \pm 0.15}$	$\mathbf{0.31/0.32 \pm 0.18}$	$\mathbf{19^{+0}_{-2}}$	$\mathbf{132^{+3}_{-2}}$	$\mathbf{132^{+3}_{-2}}$	**44**	**83**	**124**	**142**
						349	208	$0.33/0.34 \pm 0.17$	$0.33/0.34 \pm 0.17$	$0.29/0.31 \pm 0.20$	14^{+2}_{-1}	272^{+1248}_{-34}	220^{+615}_{-35}	34	68	133	188
						168	122	$0.33/0.34 \pm 0.15$	$0.33/0.34 \pm 0.15$	$0.31/0.32 \pm 0.18$	14^{+1}_{-1}	130^{+3}_{-1}	129^{+4}_{-2}	31	70	120	142
OB78	49,48,D8	0.51	9.16	13816	12265	3231	2829	$0.22/0.23 \pm 0.15$	$0.21/0.22 \pm 0.16$	$0.12/0.17 \pm 0.19$	193^{+6}_{-4}	1964^{+1149}_{-225}	1602^{+585}_{-137}	317	721	1467	2332
				1520	1463	**1438**	**1284**	$\mathbf{0.21/0.22 \pm 0.12}$	$\mathbf{0.21/0.22 \pm 0.12}$	$\mathbf{0.18/0.20 \pm 0.17}$	$\mathbf{193^{+4}_{-4}}$	$\mathbf{1321^{+5}_{-21}}$	$\mathbf{1273^{+26}_{-28}}$	**305**	**610**	**1058**	**1274**
						3231	1951	$0.19/0.21 \pm 0.14$	$0.21/0.22 \pm 0.16$	$0.12/0.17 \pm 0.19$	163^{+7}_{-7}	1743^{+801}_{-182}	1444^{+395}_{-130}	250	507	998	1603
						1438	1111	$0.19/0.20 \pm 0.12$	$0.21/0.22 \pm 0.12$	$0.18/0.20 \pm 0.17$	163^{+7}_{-7}	1291^{+21}_{-23}	1226^{+32}_{-53}	257	553	1010	1272
OB69	50	0.30	10.14	3367	3005	467	401	$0.30/0.32 \pm 0.17$	$0.29/0.32 \pm 0.18$	$0.22/0.26 \pm 0.19$	37^{+5}_{-1}	390^{+956}_{-69}	310^{+519}_{-48}	65	153	271	360
				239	223	**212**	**182**	$\mathbf{0.30/0.32 \pm 0.15}$	$\mathbf{0.29/0.32 \pm 0.16}$	$\mathbf{0.22/0.27 \pm 0.21}$	$\mathbf{37^{+5}_{-1}}$	$\mathbf{177^{+3}_{-1}}$	$\mathbf{177^{+3}_{-1}}$	**64**	**123**	**166**	**182**
						467	278	$0.29/0.31 \pm 0.17$	$0.29/0.32 \pm 0.18$	$0.22/0.26 \pm 0.19$	31^{+3}_{0}	328^{+611}_{-51}	259^{+308}_{-26}	49	95	175	248
						212	145	$0.28/0.31 \pm 0.15$	$0.29/0.32 \pm 0.16$	$0.22/0.27 \pm 0.21$	31^{+3}_{0}	176^{+1}_{0}	176^{+1}_{-5}	50	109	162	182
OB66	51,52,E1	0.48	10.37	5348	4795	516	453	$0.41/0.40 \pm 0.19$	$0.41/0.39 \pm 0.20$	$0.34/0.34 \pm 0.22$	54^{+3}_{-4}	685^{+2968}_{-136}	556^{+2324}_{-116}	104	196	324	413
				228	222	**216**	**191**	$\mathbf{0.43/0.42 \pm 0.17}$	$\mathbf{0.43/0.42 \pm 0.18}$	$\mathbf{0.34/0.42 \pm 0.20}$	$\mathbf{60^{+3}_{-5}}$	$\mathbf{179^{+4}_{0}}$	$\mathbf{179^{+4}_{0}}$	**94**	**139**	**176**	**191**
						516	306	$0.42/0.41 \pm 0.20$	$0.41/0.39 \pm 0.20$	$0.34/0.34 \pm 0.22$	43^{+1}_{-2}	538^{+2262}_{-116}	420^{+1396}_{-80}	75	124	203	272
						216	151	$0.45/0.43 \pm 0.18$	$0.43/0.42 \pm 0.18$	$0.34/0.42 \pm 0.20$	45^{+1}_{-1}	178^{+-1}_{-1}	178^{+-1}_{-1}	76	126	169	191
OB137	47	0.30	10.80	2591	2238	182	174	$0.30/0.31 \pm 0.17$	$0.30/0.31 \pm 0.17$	$0.25/0.26 \pm 0.25$	24^{+1}_{0}	165^{+745}_{-24}	137^{+368}_{-15}	39	68	115	152
				140	94	**92**	**87**	$\mathbf{0.30/0.32 \pm 0.13}$	$\mathbf{0.30/0.32 \pm 0.14}$	$\mathbf{0.41/0.37 \pm 0.26}$	$\mathbf{24^{+1}_{0}}$	$\mathbf{82^{+0}_{0}}$	$\mathbf{81^{+1}_{-1}}$	**38**	**57**	**82**	**87**
						182	130	$0.28/0.29 \pm 0.18$	$0.30/0.31 \pm 0.17$	$0.25/0.26 \pm 0.25$	18^{+1}_{-1}	138^{+435}_{-15}	114^{+196}_{-11}	31	50	84	110
						92	75	$0.28/0.31 \pm 0.14$	$0.30/0.32 \pm 0.14$	$0.41/0.37 \pm 0.26$	18^{+1}_{-1}	81^{+0}_{-1}	76^{+4}_{0}	32	53	78	87
OB54	e7,57	0.30	11.62	6535	5925	1607	1426	$0.44/0.43 \pm 0.18$	$0.43/0.42 \pm 0.19$	$0.39/0.39 \pm 0.24$	189^{+23}_{-10}	1991^{+2626}_{-294}	1733^{+2154}_{-282}	383	777	1116	1338
				797	762	**745**	**664**	$\mathbf{0.45/0.45 \pm 0.16}$	$\mathbf{0.45/0.45 \pm 0.17}$	$\mathbf{0.44/0.43 \pm 0.22}$	$\mathbf{207^{+10}_{-11}}$	$\mathbf{624^{+4}_{-5}}$	$\mathbf{624^{+4}_{-5}}$	**334**	**541**	**639**	**664**
						1607	899	$0.45/0.45 \pm 0.19$	$0.43/0.42 \pm 0.19$	$0.39/0.39 \pm 0.24$	130^{+20}_{-6}	1664^{+2079}_{-271}	1378^{+1442}_{-222}	247	500	703	847
						745	522	$0.46/0.45 \pm 0.16$	$0.45/0.45 \pm 0.17$	$0.44/0.43 \pm 0.22$	155^{+8}_{-17}	616^{+3}_{-5}	616^{+3}_{-5}	248	498	626	664
OB48S	62	0.30	11.92	7091	6194	944	865	$0.33/0.34 \pm 0.19$	$0.33/0.34 \pm 0.19$	$0.26/0.28 \pm 0.24$	87^{+0}_{-2}	805^{+2443}_{-119}	666^{+1322}_{-103}	178	364	583	778
				475	450	**436**	**403**	$\mathbf{0.33/0.35 \pm 0.16}$	$\mathbf{0.33/0.35 \pm 0.17}$	$\mathbf{0.33/0.37 \pm 0.23}$	$\mathbf{87^{+0}_{-2}}$	$\mathbf{355^{+5}_{-2}}$	$\mathbf{355^{+5}_{-2}}$	**161**	**274**	**378**	**403**
						944	544	$0.32/0.34 \pm 0.19$	$0.33/0.34 \pm 0.19$	$0.26/0.28 \pm 0.24$	79^{+1}_{-1}	674^{+1467}_{-106}	542^{+742}_{-72}	135	224	366	487
						436	319	$0.32/0.35 \pm 0.17$	$0.33/0.35 \pm 0.17$	$0.33/0.37 \pm 0.23$	79^{+1}_{-1}	352^{+3}_{-2}	351^{+4}_{-4}	138	244	366	403
OB48N	63	0.30	11.94	6664	5865	756	640	$0.27/0.29 \pm 0.17$	$0.27/0.28 \pm 0.18$	$0.20/0.25 \pm 0.22$	33^{+2}_{-2}	587^{+1463}_{-92}	468^{+756}_{-62}	84	205	375	547
				355	341	**334**	**290**	$\mathbf{0.27/0.29 \pm 0.14}$	$\mathbf{0.27/0.30 \pm 0.16}$	$\mathbf{0.29/0.32 \pm 0.22}$	$\mathbf{33^{+2}_{-2}}$	$\mathbf{284^{+-1}_{1}}$	$\mathbf{284^{+-1}_{0}}$	**75**	**164**	**246**	**290**
						756	409	$0.26/0.27 \pm 0.18$	$0.27/0.28 \pm 0.18$	$0.20/0.25 \pm 0.22$	26^{+2}_{-2}	493^{+907}_{-67}	391^{+463}_{-53}	55	123	225	352
						334	220	$0.26/0.28 \pm 0.15$	$0.27/0.30 \pm 0.16$	$0.29/0.32 \pm 0.22$	26^{+2}_{-2}	282^{+0}_{1}	278^{+3}_{-5}	57	137	238	290

Table 3
(Continued)

Region	Fields	Area[a]	Galactocentric	Sources		Stars with		$E(B-V)$ from SED Model Fitting[e]			Hot Stars with[f]			Hot Stars with[g]			
	(visits)	(kpc^2)	Distance	Total[b]	Analysis[c]	Fitted SED[d]		Hot Stars	All Stars	Cool Stars	$(M_{F439W}-M_{F555W})_o < -0.05$ mag			$T_{\rm eff} > 18$kK and $M_{F555W} <$			
			(kpc)	Sample	Sample	Tot.	$T_{\rm eff} > 18$kK	Median/Mean	Median/Mmean	Median/Mean	$M_{F555W} < -4.36$	< -2.04	< -2.254	< -4.05	< -3.25	< -2.50	< -1.65
OB51	64	0.30	11.97	4054	3644	460	380	$0.27/0.28 \pm 0.19$	$0.26/0.27 \pm 0.19$	$0.19/0.23 \pm 0.21$	21^{+1}_{-1}	337^{+887}_{-67}	247^{+430}_{-37}	50	108	195	312
				198	166	**159**	**136**	$\mathbf{0.28/0.31 \pm 0.15}$	$\mathbf{0.27/0.30 \pm 0.16}$	$\mathbf{0.26/0.28 \pm 0.19}$	$\mathbf{22^{+1}_{-1}}$	$\mathbf{136^{+0}_{-3}}$	$\mathbf{136^{+0}_{-3}}$	**37**	**77**	**114**	**136**
						460	245	$0.26/0.29 \pm 0.19$	$0.26/0.27 \pm 0.19$	$0.19/0.23 \pm 0.21$	18^{+0}_{0}	272^{+556}_{-52}	199^{+273}_{-33}	31	68	120	195
						159	107	$0.27/0.29 \pm 0.15$	$0.27/0.30 \pm 0.16$	$0.26/0.28 \pm 0.19$	18^{+2}_{0}	132^{+4}_{0}	126^{+10}_{-4}	29	67	108	136
OB59	54	0.30	12.38	3739	3349	636	565	$0.54/0.51 \pm 0.18$	$0.54/0.50 \pm 0.19$	$0.44/0.44 \pm 0.24$	153^{+19}_{-8}	973^{+2104}_{-101}	910^{+2054}_{-115}	228	369	484	545
				330	310	**305**	**269**	$\mathbf{0.56/0.52 \pm 0.17}$	$\mathbf{0.56/0.52 \pm 0.17}$	$\mathbf{0.58/0.50 \pm 0.18}$	$\mathbf{153^{+6}_{-5}}$	$\mathbf{255^{+3}_{-2}}$	$\mathbf{255^{+3}_{-2}}$	**187**	**230**	**256**	**267**
						636	413	$0.55/0.51 \pm 0.19$	$0.54/0.50 \pm 0.19$	$0.44/0.44 \pm 0.24$	109^{+16}_{-7}	851^{+1975}_{-112}	749^{+1683}_{-104}	171	257	342	395
						305	237	$0.58/0.52 \pm 0.18$	$0.56/0.52 \pm 0.17$	$0.58/0.50 \pm 0.18$	116^{+6}_{-6}	253^{+3}_{-3}	253^{+3}_{-3}	158	218	254	267
OB39	58,E8	0.30	12.45	7431	6488	613	547	$0.33/0.35 \pm 0.21$	$0.33/0.34 \pm 0.21$	$0.23/0.29 \pm 0.23$	51^{+4}_{-1}	539^{+2645}_{-95}	425^{+1480}_{-61}	118	228	378	493
				314	295	**283**	**259**	$\mathbf{0.31/0.35 \pm 0.20}$	$\mathbf{0.31/0.35 \pm 0.20}$	$\mathbf{0.23/0.32 \pm 0.26}$	$\mathbf{46^{+1}_{0}}$	$\mathbf{212^{+1}_{-4}}$	$\mathbf{212^{+1}_{-5}}$	**110**	**171**	**231**	**258**
						613	379	$0.31/0.34 \pm 0.22$	$0.33/0.34 \pm 0.21$	$0.23/0.29 \pm 0.23$	45^{+2}_{-1}	429^{+1640}_{-65}	341^{+822}_{-41}	87	151	247	337
						283	213	$0.29/0.34 \pm 0.21$	$0.31/0.35 \pm 0.20$	$0.23/0.32 \pm 0.26$	39^{+2}_{-2}	208^{+3}_{-2}	204^{+6}_{-4}	94	157	224	258
OB41	60,F0	0.30	12.57	7872	7005	899	778	$0.26/0.28 \pm 0.18$	$0.26/0.28 \pm 0.20$	$0.24/0.31 \pm 0.26$	68^{+2}_{-1}	614^{+1477}_{-66}	519^{+731}_{-51}	139	274	476	655
				462	446	**434**	**384**	$\mathbf{0.25/0.28 \pm 0.16}$	$\mathbf{0.25/0.28 \pm 0.17}$	$\mathbf{0.32/0.34 \pm 0.25}$	$\mathbf{67^{+0}_{-3}}$	$\mathbf{373^{+0}_{-1}}$	$\mathbf{371^{+1}_{-10}}$	**125**	**227**	**331**	**378**
						899	558	$0.22/0.25 \pm 0.18$	$0.26/0.28 \pm 0.20$	$0.24/0.31 \pm 0.26$	61^{+1}_{-3}	544^{+907}_{-50}	460^{+456}_{-54}	96	184	320	460
						434	326	$0.23/0.26 \pm 0.16$	$0.25/0.28 \pm 0.17$	$0.32/0.34 \pm 0.25$	60^{+1}_{-5}	370^{+1}_{-5}	354^{+8}_{-16}	106	205	322	378
OB42	61	0.30	12.74	7514	6645	967	869	$0.34/0.35 \pm 0.19$	$0.34/0.35 \pm 0.19$	$0.27/0.31 \pm 0.23$	119^{+6}_{-5}	865^{+2763}_{-124}	722^{+1604}_{-96}	191	392	625	774
				525	491	**480**	**436**	$\mathbf{0.33/0.35 \pm 0.16}$	$\mathbf{0.33/0.35 \pm 0.17}$	$\mathbf{0.35/0.37 \pm 0.22}$	$\mathbf{110^{+6}_{-3}}$	$\mathbf{396^{+3}_{-3}}$	$\mathbf{396^{+3}_{-3}}$	**173**	**306**	**408**	**433**
						967	567	$0.32/0.34 \pm 0.19$	$0.34/0.35 \pm 0.19$	$0.27/0.31 \pm 0.23$	97^{+3}_{-3}	721^{+1718}_{-88}	594^{+878}_{-70}	136	261	403	500
						480	335	$0.31/0.34 \pm 0.16$	$0.33/0.35 \pm 0.17$	$0.35/0.37 \pm 0.22$	92^{+2}_{-2}	389^{+3}_{2}	388^{+4}_{-3}	141	274	399	433
OB40	59	0.30	12.94	7953	6965	865	780	$0.30/0.33 \pm 0.19$	$0.30/0.33 \pm 0.19$	$0.25/0.29 \pm 0.22$	84^{+4}_{-3}	667^{+2190}_{-104}	540^{+1143}_{-59}	162	349	529	697
				481	432	**420**	**381**	$\mathbf{0.29/0.32 \pm 0.17}$	$\mathbf{0.29/0.32 \pm 0.17}$	$\mathbf{0.35/0.34 \pm 0.20}$	$\mathbf{79^{+3}_{-1}}$	$\mathbf{344^{+1}_{-1}}$	$\mathbf{344^{+1}_{-4}}$	**145**	**269**	**340**	**378**
						865	521	$0.27/0.31 \pm 0.19$	$0.30/0.33 \pm 0.19$	$0.25/0.29 \pm 0.22$	70^{+2}_{-2}	552^{+1306}_{-65}	471^{+645}_{-52}	120	220	335	459
						420	305	$0.27/0.31 \pm 0.17$	$0.29/0.32 \pm 0.17$	$0.35/0.34 \pm 0.20$	67^{+0}_{-3}	341^{+2}_{-5}	336^{+5}_{-9}	119	245	333	378
OB33	56	0.30	13.20	8293	7371	664	591	$0.39/0.39 \pm 0.18$	$0.39/0.39 \pm 0.19$	$0.38/0.37 \pm 0.22$	77^{+6}_{0}	792^{+4510}_{-135}	668^{+3120}_{-125}	140	289	448	560
				298	291	**285**	**253**	$\mathbf{0.40/0.41 \pm 0.16}$	$\mathbf{0.40/0.41 \pm 0.16}$	$\mathbf{0.38/0.38 \pm 0.20}$	$\mathbf{81^{+3}_{-2}}$	$\mathbf{235^{+2}_{-2}}$	$\mathbf{235^{+2}_{-2}}$	**121**	**199**	**246**	**253**
						664	358	$0.42/0.42 \pm 0.18$	$0.39/0.39 \pm 0.19$	$0.38/0.37 \pm 0.22$	67^{+5}_{-1}	650^{+3099}_{-120}	524^{+1774}_{-84}	103	182	284	343
						285	189	$0.42/0.42 \pm 0.16$	$0.40/0.41 \pm 0.16$	$0.38/0.38 \pm 0.20$	72^{+2}_{-4}	230^{+2}_{-2}	230^{+2}_{-2}	107	188	245	253
OB136	45	0.30	15.32	2514	2265	318	270	$0.37/0.37 \pm 0.17$	$0.36/0.35 \pm 0.18$	$0.21/0.25 \pm 0.23$	29^{+2}_{-3}	356^{+1146}_{-56}	296^{+788}_{-61}	48	107	183	246
				158	139	**135**	**115**	$\mathbf{0.39/0.40 \pm 0.13}$	$\mathbf{0.39/0.39 \pm 0.15}$	$\mathbf{0.33/0.32 \pm 0.22}$	$\mathbf{31^{+1}_{0}}$	$\mathbf{120^{+1}_{0}}$	$\mathbf{120^{+1}_{0}}$	**44**	**83**	**109**	**115**
						318	178	$0.36/0.37 \pm 0.17$	$0.36/0.35 \pm 0.18$	$0.21/0.25 \pm 0.23$	21^{+0}_{-1}	293^{+806}_{-55}	222^{+501}_{-40}	30	56	112	160
						135	88	$0.38/0.38 \pm 0.14$	$0.39/0.39 \pm 0.15$	$0.33/0.32 \pm 0.22$	24^{+0}_{0}	119^{+0}_{-1}	119^{+0}_{-1}	32	72	106	115
OB99	65	0.30	15.50	2698	2468	496	442	$0.23/0.24 \pm 0.15$	$0.23/0.24 \pm 0.16$	$0.25/0.28 \pm 0.20$	30^{+3}_{-1}	328^{+457}_{-43}	261^{+219}_{-28}	54	111	233	367
				240	228	**222**	**192**	$\mathbf{0.24/0.26 \pm 0.13}$	$\mathbf{0.24/0.27 \pm 0.14}$	$\mathbf{0.30/0.33 \pm 0.18}$	$\mathbf{33^{+0}_{-2}}$	$\mathbf{190^{+0}_{-3}}$	$\mathbf{185^{+3}_{-2}}$	**50**	**98**	**167**	**190**
						496	266	$0.23/0.24 \pm 0.16$	$0.23/0.24 \pm 0.16$	$0.25/0.28 \pm 0.20$	24^{+1}_{-1}	285^{+295}_{-40}	229^{+136}_{-23}	37	72	142	221
						222	149	$0.23/0.25 \pm 0.13$	$0.24/0.27 \pm 0.14$	$0.30/0.33 \pm 0.18$	26^{+1}_{-1}	186^{+2}_{-4}	182^{+1}_{-5}	39	87	157	190

Table 3
(Continued)

Region	Fields	Area[a]	Galactocentric	Sources		Stars with		$E(B-V)$ from SED Model Fitting[e]			Hot Stars with[f]			Hot Stars with[g]			
	(visits)	(kpc^2)	Distance	Total[b]	Analysis[c]	Fitted SED[d]		Hot Stars	All Stars	Cool Stars	$(M_{F439W}-M_{F555W})_o < -0.05$ mag			$T_{\rm eff} > 18$kK and $M_{F555W} <$			
			(kpc)	Sample	Sample	Tot.	$T_{\rm eff} > 18$kK	Median/Mean	Median/Mmean	Median/Mean	$M_{F555W} < -4.36$	<-2.04	<-2.254	<-4.05	<-3.25	<-2.50	<-1.65
OB102	66	0.30	16.09	3018	2789	1052	973	$0.28/0.28 \pm 0.15$	$0.28/0.28 \pm 0.15$	$0.24/0.25 \pm 0.22$	90^{+4}_{-3}	859^{+666}_{-110}	730^{+400}_{-81}	136	328	607	866
				530	513	**507**	**473**	$\mathbf{0.28/0.29 \pm 0.12}$	$\mathbf{0.28/0.29 \pm 0.13}$	$\mathbf{0.30/0.33 \pm 0.18}$	$\mathbf{89^{+3}_{-3}}$	$\mathbf{460^{+5}_{-3}}$	$\mathbf{458^{+7}_{-5}}$	**130**	**283**	**423**	**472**
						1052	626	$0.27/0.26 \pm 0.15$	$0.28/0.28 \pm 0.15$	$0.24/0.25 \pm 0.22$	74^{+5}_{-1}	751^{+450}_{-85}	632^{+254}_{-75}	104	201	358	558
						507	368	$0.27/0.27 \pm 0.12$	$0.28/0.29 \pm 0.13$	$0.30/0.33 \pm 0.18$	73^{+4}_{-1}	455^{+4}_{-4}	447^{+9}_{-9}	107	247	405	472
OB139	46	0.30	16.36	2427	2245	485	455	$0.41/0.41 \pm 0.16$	$0.41/0.40 \pm 0.16$	$0.34/0.34 \pm 0.22$	73^{+2}_{-2}	512^{+1277}_{-59}	461^{+1013}_{-71}	122	237	371	426
				267	262	**259**	**247**	$\mathbf{0.41/0.43 \pm 0.13}$	$\mathbf{0.41/0.43 \pm 0.14}$	$\mathbf{0.34/0.39 \pm 0.20}$	$\mathbf{71^{+1}_{-2}}$	$\mathbf{229^{+2}_{-2}}$	$\mathbf{229^{+2}_{-2}}$	**118**	**198**	**245**	**247**
						485	264	$0.43/0.42 \pm 0.16$	$0.41/0.40 \pm 0.16$	$0.34/0.34 \pm 0.22$	60^{+1}_{-9}	453^{+979}_{-72}	384^{+643}_{-40}	83	136	209	249
						259	166	$0.43/0.43 \pm 0.14$	$0.41/0.43 \pm 0.14$	$0.34/0.39 \pm 0.20$	58^{+0}_{-8}	227^{+1}_{-5}	227^{+1}_{-5}	87	178	242	247
OB157	67,f7	0.30	20.93	914	745	161	138	$0.27/0.26 \pm 0.16$	$0.27/0.27 \pm 0.17$	$0.27/0.30 \pm 0.24$	6^{+1}_{0}	121^{+202}_{-23}	91^{+102}_{-17}	11	31	68	106
				94	59	**56**	**49**	$\mathbf{0.27/0.28 \pm 0.12}$	$\mathbf{0.28/0.29 \pm 0.13}$	$\mathbf{0.33/0.38 \pm 0.21}$	$\mathbf{6^{+0}_{0}}$	$\mathbf{48^{+0}_{0}}$	$\mathbf{48^{+0}_{0}}$	**11**	**25**	**45**	**48**
						161	90	$0.25/0.25 \pm 0.14$	$0.27/0.27 \pm 0.17$	$0.27/0.30 \pm 0.24$	4^{+2}_{0}	98^{+126}_{-20}	72^{+70}_{-16}	6	21	37	69
						56	40	$0.25/0.27 \pm 0.11$	$0.28/0.29 \pm 0.13$	$0.33/0.38 \pm 0.21$	5^{+0}_{-1}	48^{+0}_{0}	46^{+2}_{0}	6	21	40	48
OB184	44	0.30	21.90	1247	1060	320	295	$0.14/0.15 \pm 0.13$	$0.14/0.15 \pm 0.13$	$0.05/0.10 \pm 0.12$	19^{+1}_{0}	151^{+87}_{-10}	133^{+29}_{-5}	35	56	111	217
				194	159	**151**	**139**	$\mathbf{0.15/0.14 \pm 0.10}$	$\mathbf{0.14/0.14 \pm 0.10}$	$\mathbf{0.08/0.09 \pm 0.09}$	$\mathbf{19^{+1}_{0}}$	$\mathbf{132^{+5}_{-4}}$	$\mathbf{122^{+4}_{-2}}$	**35**	**55**	**98**	**135**
						320	234	$0.13/0.14 \pm 0.12$	$0.14/0.15 \pm 0.13$	$0.05/0.10 \pm 0.12$	17^{+0}_{-1}	143^{+58}_{-7}	128^{+22}_{-5}	32	48	96	175
						151	134	$0.14/0.14 \pm 0.10$	$0.14/0.14 \pm 0.10$	$0.08/0.09 \pm 0.09$	17^{+0}_{-1}	128^{+5}_{-3}	120^{+3}_{-3}	34	51	94	135

Notes. Number of hot stars, and average extinction in the regions.

[a] The area for a WFPC2 field is 20554.2 $arcsec^2$; for the two fields in OB78, accounting for overlap, the total area is 35010.4 $arcsec^2$, and for OB66 is 32897 $arcsec^2$.

[b] Total sources detected in either F555W or F439W plus at least another filter.

[c] Number of sources detected in F555W plus at least another filter, with *HSTphot* type = 1 and $-0.3 <$ *sharpness* < 0.3. This is the analysis sample.

[d] Sources (out of the analysis sample) with error cuts of <0.3,0.3,0.3 mag (first row) and <0.15/0.1/0.1 mag (second row) in F336W/F439W/F555W. The third and fourth rows repeat the first and second ones, as for error cuts, but excluding stars with suspicious UV photometry which causes bad fitting results (discussed in Sections 4.2 and 5).

[e] Derived from SED fitting in Section 4; in conspicuous star-forming regions hot stars are the majority of the sample.

[f] For a 4 Myr old population, the first two $M_{\rm F555W}$ limits correspond to stars with initial mass of >20 and 9 $M_\odot$; the third selection corresponds to mass >9 $M_\odot$ on a 10 Myr isochrone. Most fields include a mix of populations within these ages, as indicated by the large "+" errors (see text). See Section 5.2.

[g] Number of stars hotter than 18,000 K and brighter than $M_{\rm F555W}$ limits corresponding to B0V, B1V, B2V, and B3V, respectively. The stringent error cuts limits the completeness to an earlier spectral type, to an extent depending on local extinction.

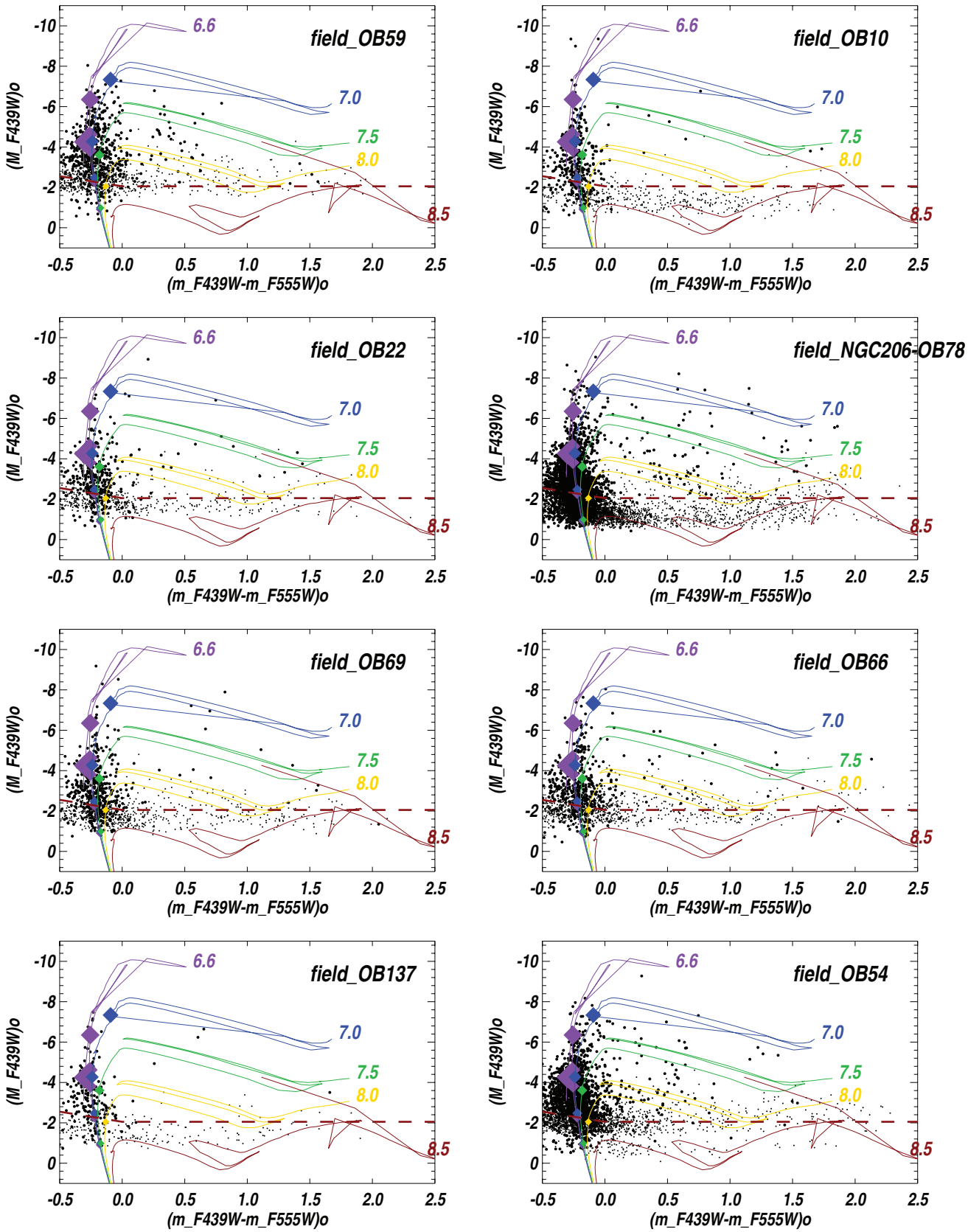

Figure 8. HRD and isochrones, for each star-forming region. Large dots mark sources with good photometry in several filters, for which a value of $E(B-V)$ was derived; the others are corrected for reddening using the average value for the region. NGC 206 and OB66 were covered with two WFPC2 fields, the other diagrams enclose one WFPC2 field each. The average completeness limit is shown (dashed line); for OB78, which has lower reddening than other regions, the photometry reaches a deeper limit. Diamonds (smallest to largest) mark the position of a star with *initial* mass of 5, 9, 15, 20, 40, and 60 $M_{\odot}$, on each isochrone (age labeled in log yr). The term "field_OB. . ." is used to remind that we include in these diagrams not just the stars within the contour of the targeted OB association, but all stars in its WFPC2 field. More panels are shown in the online journal.

(An extended, color version of this figure is available in the online journal.)

age spread), but it excludes evolved stars such as red supergiants on the 10 Myr isochrone. In sum: *if* all stars were on a few Myr isochrone, the counts in Table 3 (columns 12 and 13) would give the number of stars with initial mass >20 and >9 $M_{\odot}$. But where there is a substantial mix of ~10 Myr populations, the more massive star counts are upper limits. For dwarf irregular galaxies, where the star formation is episodical, and few Myr old populations are seen with $\sim 10^8$ yr populations, the stars on the younger isochrones are often well separated from the older ones (Bianchi et al. 2012). In our M31 fields, star formation seems to have been ongoing more regularly.

The uncertainty in the massive star counts given in Table 3 was estimated by recounting the stars after adding, and subtracting from each, its photometric error (1σ). When this number is very large (even larger than the source counts obtained using the nominal photometry), it indicates that the blue plume is wide, at the magnitude cut of the chosen mass, either due to photometric errors and/or to substantial presence of older populations whose isochrones run very close in this color choice. The uncertainties are very small for the brighter $M_{\rm F555W}$ cut, (corresponding to higher masses), where isochrones of older ages are well separated, massive stars having evolved away from the main sequence. In these counts, and the following analysis, for each star with SED fitting we adopted the results with the metallicity and extinction type that gives the smallest χ^2 minimum.

Again we recall that for a fraction of the sample $T_{\rm eff}$ is likely overestimated, as discussed in the previous section, due to uncertainties in the UV photometry. For this reason, we also give in Table 3 the stellar counts and average reddening obtained by excluding these stars from the sample. In practice, it is likely that these stars are hot, given that they are detected in UV filters, and therefore excluding them from hot stellar counts may give lower limits. On the other hand, they are too many to be very hot: the reduction in the number of hot stars with initial mass >9 $M_{\odot}$, for example, if we exclude these stars (compare the second and fourth rows for each field in Table 2), is between 12% and 26% for most fields, except for OB 136 and OB 157 (much higher, but less significant given the low numbers), and for OB 184 where there are almost no such cases. Further examination of these sources is deferred to a future analysis combining the deeper photometry in the *U*-band from the PHAT survey (Dalcanton et al. 2012), which will be available for a subset of our fields. For the analysis that follows, we count them in the hot-star census.

5.2. Definition of OB Associations and Spatial Clustering Properties of the Young Stars

We selected the stars hotter than 18,000 K in each field (or contiguous fields), and looked for spatial clustering by using a nearest-neighbor association algorithm. Two stars are deemed associated if their projected distance in the sky is closer than a given value, which we term "link-distance." A small link-distance will define only the most compact clusters; increasing the link-distance will result in more inclusive, and lower density, regions to be defined. The other important parameter to be chosen is the minimum number of stars in an association that we want to consider; given the superb *HST* resolution, which allows us to examine even small structures, we adopt a minimum number of four "linked" hot stars, to catalog them as an association. Of course, the choice of the $T_{\rm eff}$ limit (or color selection, in similar methods) influences the number of stars selected, and the resulting associations, and consequently, uncertainties in $T_{\rm eff}$ derivation propagate on the results. However, random uncertainties will cancel out in the characterization of a large sample of associations, and as we see in Figure 9, a robust and interesting picture emerges.

Our fields cover selected individual regions, and not large contiguous areas; therefore we do not perform a search for preferred frequencies in spatial clustering, as we did in Kang et al. (2009) for the whole galaxy because it would not be meaningful on separate areas, but also because the *HST* resolution gives much more detail than the ground-based catalog, and actual clustering scales "preferred" by the stars, if any, may vary with location and are not uniform across such a big galaxy. Instead, we examine a range of spatial frequencies in each location.

5.2.1. Selection of Hot Stars and Completeness of Stellar Counts

Before we look at the clustering results, some considerations regarding the methodology are useful. The first important consideration when applying clustering-detection algorithms to hot massive stars, concerns the selection of the hot stars' sample, and its completeness and possible contamination. The "hot-star" selection was done here by choosing all the stars with $T_{\rm eff} \gtrsim$ 18,000 K, as derived from SED fitting (Section 4.2). This temperature corresponds to spectral type ~B3V. Our original minimum completeness goal of ~B0V for this survey is met in all fields, and exceeded where reddening is not too high. We can assess in more detail the completeness to various stellar masses, as follows. A B0V/B1V/B2V/B3V star has $M_V = -4.0/-3.2/-2.45/-1.6$ mag (Aller et al. 1982), which becomes, using the transformation from V to $m_{\rm F555W}$ from our model colors for hot stars ($V - m_{\rm F555W} = 0.05$), $m_{\rm F555W} = 20.42/21.22/21.97/22.82 + (E(B-V) \times R_V)$ mag, at the distance of M31. All these values are brighter than our photometry completeness limit of $m_{\rm F555W} = 22.9$ mag (Section 3.1) in absence of reddening. On the other hand, we want to chose subsamples with stringent enough error cuts so that intruders are minimized in the selected sample. In Table 3 we give number counts of stars hotter than 18,000 K and brighter than the above absolute magnitude limits, i.e., earlier than B0–B3 on the main sequence, in the last four columns. As explained in the previous section, we also give counts of stars more massive than 20 and 9 $M_{\odot}$ (initial mass) using the corresponding brightness limits for a 4 Myr population, and >9 $M_{\odot}$ also assuming the corresponding limit on a 10 Myr isochrone. The comparison among the two latter counts is an indication of the unavoidable uncertainty that a possible age spread (presence of different young populations in the same region) will introduce, as discussed above, which is reflected by the uncertainties in the counts.

For each region we give stellar counts within the above limits of magnitude/color (or magnitude/$T_{\rm eff}$), including all stars detected in at least three bands (F336W, F439W, and F555W), in the first row, and including only stars with errors <0.15/0.1/0.1 mag in these three filters, respectively (second row for each region in Table 3). The comparison between the numbers in the first and second rows, in the last four columns, shows that the "loss" of B0V stars due to the more stringent error cuts is less than ~10% in most fields (except for OB51: ~25%, and OB59: 18%) and is zero or negligible in OB157, OB184, OB69, and OB78, i.e., in the fields with the lowest extinction and/or more populated young isochrones. In the "clean" sample, with stringent error cuts, the decrease in <B1V star counts is still less than 30% for 17 out of 22 regions, the reduction of <B2V counts is less than 60% for half of the regions, and <B3V counts decrease by a factor of $\lesssim$2. For the outermost

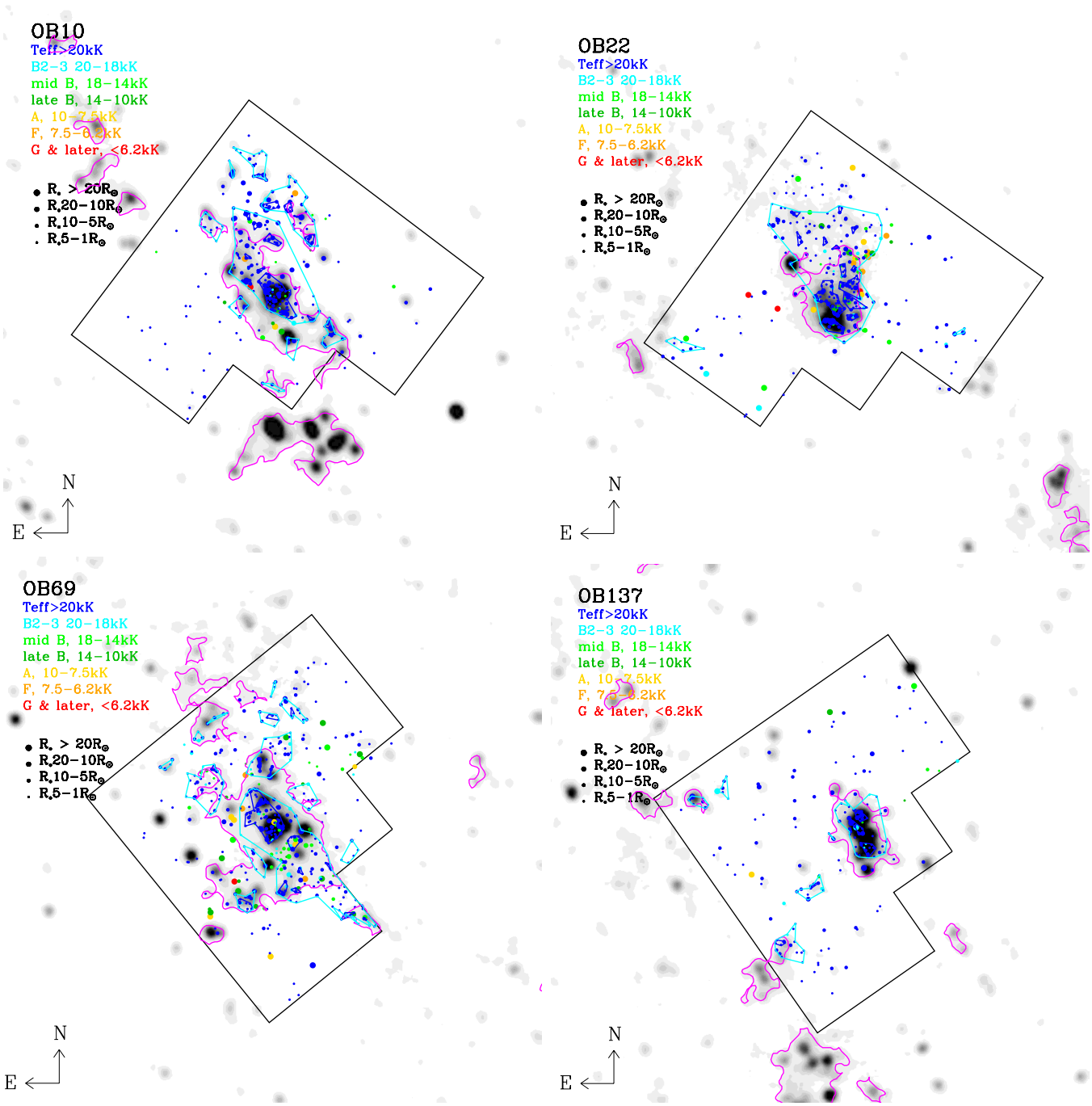

Figure 9. Overlaid on a *GALEX* FUV image are the brightest stars (an approximate footprint of the WFPC2 field is shown). Stars are color coded by $T_{\rm eff}$; the dots size is proportional to the stellar radius (parameters from SED fitting). Magenta contours are the *GALEX*-defined star-forming regions from Kang et al. (2009), blue and cyan contours are OB associations defined in this work (Section 5.2) with a link-distance of 3 and 6 arcsec, respectively (the link-distance is the maximum allowed separation between stars to be deemed "associated") and a minimum number of four hot stars. OB 10 and OB 22 (fields 55 and 53) are in the inner spiral structure, NE and SW, respectively. OB 69 and OB 137 (fields 50 and 47) are next when progressing outward in galactocentric distance in the SW quadrant. Numerous intermediate $T_{\rm eff}$ stars (green dots) are also crowding in the dense regions, they are not visible in the most crowded regions because they are plotted underneath the hot stars (blue dots). Panels for the other regions are shown in the online journal.

(The complete figure set (4 images) is available in the online journal.)

region OB184, which has the least extinction, the sample is basically complete down to B2V, even with the stringent error cuts. However, such "losses" of stellar counts (decrease of the number) in the selection locus, when error cuts are applied, are not necessarily a real loss of stars of the chosen spectral types, because the selection from the sample with large photometric errors includes many "false" positives. Since the IMF is skewed toward lower masses, photometric errors, although intrinsically random, have the effect of augmenting the number of counts (the more numerous low-mass stars moving above the magnitude cut when the photometric error is subtracted). Therefore such "losses" in fact only represent upper limits to the fraction of actual qualifying stars that may be missed, and part or rather most of the count reduction is due to the elimination of intruders.

Based on these assessments, we chose to derive the clustering properties for a "clean sample" with errors <0.15/0.1/0.1 mag

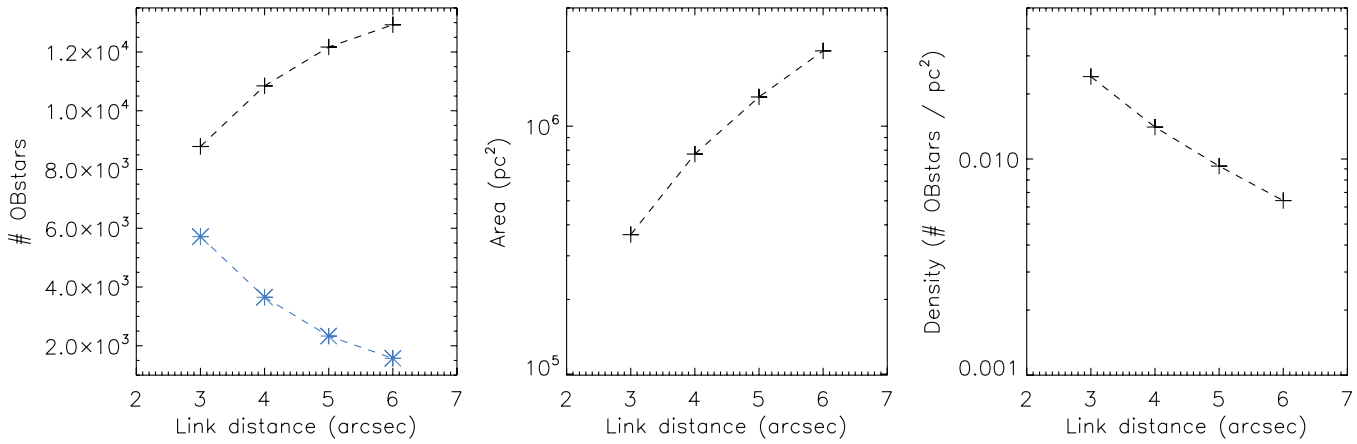

Figure 10. Left: the number of hot stars included in associations (black plus symbols) increases with link-distance, steeply for small values, then flattens out when the scales of spiral arms are reached. The figure plots the total number for the whole sample. Figure 9 shows the effect of link-distance in individual environments. Blue (cross) symbols give the number of hot stars not included in OB associations. Middle and right: the area included in defined associations and density of hot stars depend on the adopted link-distance.

(A color version of this figure is available in the online journal.)

in $m_{\rm F336W}$, $m_{\rm F439W}$, and $m_{\rm F555W}$, respectively, to avoid sources with large uncertainties; these restrictions make our hot-star selection very complete down to spectral types of B3V to B0V, from the least to the most reddened region. Previous studies usually define as "complete" a sample with 50% completeness; in this definition, we would reach B3V across the whole sample. Our completeness limit for hot-star selection is deeper than in previous studies, which chose for example a limit of $M_V < -4.5$ mag and $(B-V)_o < 0.5$ mag (e.g., Bresolin et al. 1998; Bastian et al. 2009 for M33), but also used photometric catalogs shallower than our catalog. We also have in this study the advantage of applying individual reddening corrections to each region (from SED-fitting) rather than an average value, and of the *HST* resolution. In addition, we note that our limits of $T_{\rm eff}$ and absolute magnitude defining the hot stars subsample (for clustering analysis) are approximately consistent with the same spectral type (or mass) limit, while the $(B-V)_o <$ 0.5 mag color limit used in previous studies includes a greater contamination by older populations; therefore their magnitude limit corresponds to a highly varying mass limit, across the sample. Of course, a more stringent color limit, which makes the selection more consistent in spectral type with the magnitude limit, will also leave out some massive evolved stars. However, we see from the HRDs (Figure 8) that the number of evolved stars not counted is always much less than the number of intruders that would be included by a wider limit. A star with initial mass ∼15–20 $M_\odot$ will still be on the main sequence at 10 Myr of age and a B3V star will remain on the main sequence for ∼45 Myr. Therefore our selection of stars hotter than 18,000 K includes a significant representation of the massive star counts for the young populations.

5.2.2. The Properties of the OB Associations

The results are shown in Figure 9, where in the WFPC2 fields the bright stars are color-coded according to their derived $T_{\rm eff}$ (and radius). We overplot contours of the OB associations derived from the clustering algorithm, from the *HST* photometry, for two sample link-distances of 3 and 6 arcsec (11.4 and 22.8 pc at M31's distance), in blue and cyan colors, respectively. The clustering within rich star-forming regions shows that young populations are structured hierarchically, on various levels of compactness, sampled by different spatial scales: dense small clumps of hot stars are arranged within broader complexes of lower density. We show results only with these two values of link-distance, for clarity, across the whole sample; they provide a comprehensive definition of the structures seen in most fields; however, in the richest star-forming sites such as NGC 206, structures are clearly seen on more compact scales as well (Figure 9). In these maps, hotter stars are plotted above cooler ones: numerous intermediate $T_{\rm eff}$ stars are present in the same regions where the hotter stars crowd, but are not visible because they are covered by the blue dots (hot stars).

Such hierarchical fragmentation has been postulated and discussed before (e.g., Elmegreen 2006, 2008; Bastian et al. 2009); this study allows us to examine quantitatively the distribution of the associations across star-forming regions over large galactocentric distances, at the *HST* resolution which is necessary in the crowded sites where many compact star groups are unresolved in ground-based imaging (e.g., Bianchi et al. 2012 for a comparison). The physical characteristics of the associations reflect the result of the star formation process, from the fragmentation of the parent molecular cloud, and of the dynamical evolution in the galaxy disk. With time, the wind momentum and radiation from the young massive stars blows away most of the remaining dust and gas, and the associations (unbound) become less compact and eventually dissolve within the general galaxy potential (e.g., Bastian et al. 2011 and references therein).

The total number of hot stars included in OB associations of course increases with larger link-distances; results for link-distances of 3″, 4″, 5″, and 6″ are shown in Figures 10 and 11; the density of stars included (average of all associations) correspondingly decreases: 0.0313, 0.0157, 0.0100, and 0.0076 pc^{-2}, respectively. The figure shows (first panel) how the number of stars included in associations increases steeply over those excluded by the clustering criterion, with progressively larger link-distances. We caution that the density of non-clustered hot stars (field stars) cannot be estimated from these data, since our fields are largely occupied by star-forming complexes. The ratio of hot stars in clusters over "field" stars will be better determined from the large area coverage provided by the PHAT survey (Dalcanton et al. 2012). Such ratio was also estimated by Kang et al. (2009) over the M31 disk, but the results were limited by the depth of the LGGS survey (see Bianchi et al.

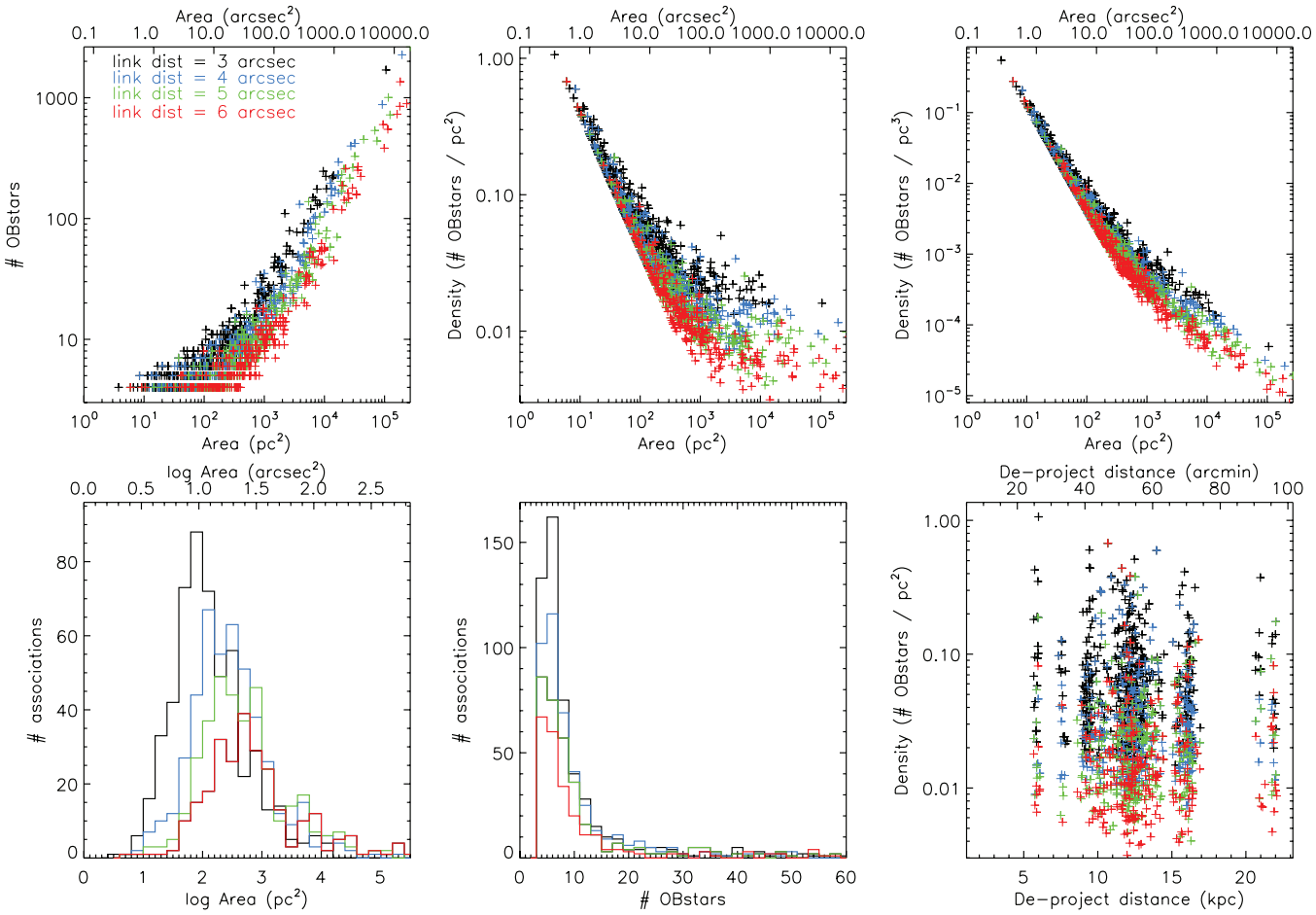

Figure 11. Top: number counts, and density, of hot stars in *HST*-defined associations. The density is shown as projected on the sky (pc^{-2}, middle panel), and as pc^{-3}, assuming that the volume of each region is equal to its $area^{3/2}$ (right panel). The lower envelope arises from our choice of a minimum number of four hot stars for an association to be recorded. Bottom: distribution of areas and hot-star content. The peaks in the area distribution (bottom left) roughly correspond to an area ≈link-distance^2, and are due to the highest number of associations having the minimum number of hot stars (4) to be included in our catalog. The last panel shows the projected density as a function of galactocentric distance: each region shows a wide range, and the density varies by >1 dex with the assumed link-distance, but also by >1 dex from the "10 kpc ring" to the outermost regions.

2012 for a comparison) and by the spatial resolution >10 times worse than *HST*, both effects making the hot-star counts from ground-based surveys a lower limit.

Figure 11 (lower plots) shows that the areas of our OB associations are mostly between $\sim 10^2$ and 10^3 pc^2; the distribution is skewed toward larger or smaller sizes depending on the adopted link-distance. The peak in the area distribution corresponds to an area roughly equal to link-distance^2, reminding us that "preferred" sizes found in any given work may be at least partly due to the resolution of the data and of the method. The lower right panel of Figure 11 shows that most associations contain four hot stars, the minimum number that we chose as a criterion for including an association in the present catalog. The top panels of Figure 11 show distributions of the number of hot stars, and their density, with the area of the associations. The lower envelope in the data points reflects our adopted minimum number of stars for an association to be cataloged. The relations vary quantitatively with link-distance, as expected: a shift in the distribution of number of stars with area (upper left panel), a change in slope and spread in the density of hot stars. But in all cases, smaller regions tend to be decidedly more compact (denser). While we are counting stars and measuring the area of an association projected on the sky in two dimensions in order to get an idea of the actual stellar density (three dimensions) we also plot in the upper right panel the spatial density, dividing the number of hot stars by a volume assumed equal to $area^{(3/2)}$. This is an arbitrary approximation for each single complex, but it should give a statistical slope of the distribution, since associations would have random orientations and shapes. A comparison with previously defined OB associations, from ground-based data (van den Bergh 1964) and with *GALEX* data (resolution 4.″2 in far-UV) is only possible for *HST*-defined associations with large link-distances ($\gtrsim 6''$).

Now we can come back to the question of whether young star clustering happens on preferred spatial scales, and whether these depend on environment (and/or age, and dynamical factors). It has become clear since the work of Hodge (1986a) that sizes and number of defined OB associations in galaxies depend on the characteristics of the observational data used. Hodge (1986a) compared data of associations in different galaxies from the Magellanic Clouds to beyond the Local Group, and showed that results largely correlate with the distance of the galaxies, demonstrating the effects of resolution and depth of the imaging on the detection and definition of OB associations; real differences among galaxy types are therefore difficult to quantify given the problem of identifying associations in a consistent way in different galaxies. Such dependence of the defined associations on the data quality, and on the method,

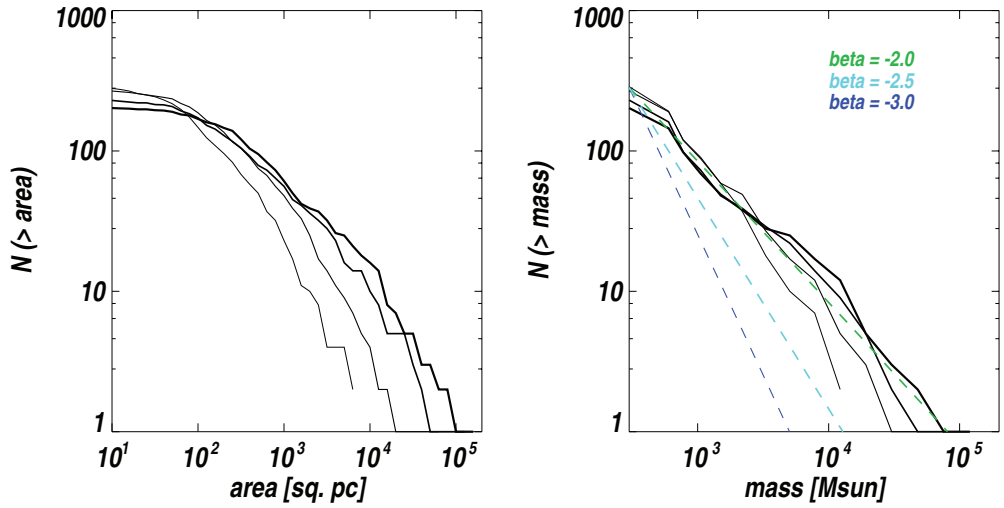

Figure 12. Cumulative distribution of areas of the *HST*-defined OB associations (left) and of their masses (right; masses are derived from the massive-star counts extrapolated with an IMF) Results are shown for link-distances of 3″, 4″, 5″, and 6″ (thinnest to thickest lines). The areas show a log-normal distribution in the central part of the explored range, and the mass distribution a power law (roughly) with slope depending on the adopted link-distances. Dashed lines show some power laws ($dN/dM_{\rm cl} \approx {M_{\rm cl}}^{\beta}$) with $\beta = -2, -2.5, -3.0$ as a visual reference (see discussion).

(A color version of this figure is available in the online journal.)

prevented the use of their size distributions as distance indicators (as had been suggested, e.g., by Wray & de Vaucouleurs 1980). That defined associations depend on criteria and data used is similarly evident from quantitative definitions on modern data. Bastian et al. (2009) argue that there is no intrinsically preferred scale for clustering, from examining the LGGS catalog in M33. Our *HST* resolution allows a better exploration of the smallest scales, on one hand, and is limited to scales smaller than the field size (600 pc) on the other hand. It shows that, within this range, clustering does not have a decidedly preferred scale but different hierarchical layers can be detected by allowing different densities (or in other words, choosing different link-distances). However, a broad spectrum of structuring level across our sampled environments is evident from Figure 9.

A caveat in this type of analysis is the difficulty of distinguishing physical associations from chance alignments (asterisms) when only imaging is available and there is no kinematics information. False identifications (asterisms included in cluster catalogs) are more likely for small stellar clusters than for large complexes. However, two nearby structures would be counted as one massive association if aligned on close sightlines, or as two separate structures if they had the same physical separation, but were aligned in the plane of the sky. This problem would affect "by-eye" or quantitative methods in the same way, and cause more high-mass cases in the measured catalog than in the real mass distribution. It would be smallest for face-on galaxies since star formation is largely confined to the disk.

Figure 12 (left) shows the cumulative distribution of the regions with area (we use area rather than a linear size because of the great variety of shapes among the associations' contours). The distributions, given for various link-distances, appear similar to previously found log-normal distributions (e.g., Bastian et al. 2009). They can be approximated by a power law, with slope depending on the chosen link-distance, in the central range sampled, with areas between 100 and 10,000 pc^2. The right-side plot in the same figure shows the cumulative distribution of masses. Masses are derived by extrapolating hot-star counts with a Kroupa (2001) IMF, and assuming that our sample of hot stars is complete down to the initial mass of ∼B2V types; the uncertainty from possible incompleteness would cause a shift: if the actual mass limit of the massive-star counts were lower or higher, the curves in Figure 12 (right) would slightly shift horizontally. However, if the bias were mass-dependent and not uniform (as, e.g., the binary fraction), the shape of the distribution may be slightly affected, since a number or associations may shift to higher or lower mass bins.

The choice of link-distance has an effect on the definition of OB associations, as discussed and as shown in Figure 9, and affects the resulting slope of the cumulative distribution. Another bias in the mass estimate may come from unresolved binaries composed of two hot stars, which is known to be a frequent case: these may appear as a single hot star in the photometry, causing an underestimate of the star counts and correspondingly of the mass.

5.3. Comparison with GALEX-defined Star-forming Regions

In Figure 9 we also overplot contours of the star-forming regions defined from *GALEX* far-UV fluxes (magenta color) by Kang et al. (2009). The first notable result is that in all cases the *GALEX* selection did not miss any hot-star presence, even sparse. Thanks to *GALEX*'s very deep sensitivity, its low resolution does not affect the detection and selection of young populations, even in reddened regions.

We also counted the hot stars within each *GALEX* far-UV-defined star-forming region and *HST*-defined OB association. Because Kang et al. (2009) used a homogeneous flux threshold to define UV-regions across the whole galaxy, necessary for a consistent global study, in the brightest portions of spiral arms contiguous star-forming complexes are merged into one large structure and the *GALEX*-defined contour is larger than the area covered by an *HST* field (using a higher *GALEX* flux threshold would separate the brightest regions into substructures, but would miss many fainter regions). Therefore, we compared the number of hot stars within each contour, with integrated *GALEX* measurements, only for the regions that are totally or mostly enclosed in our fields. The number of hot stars

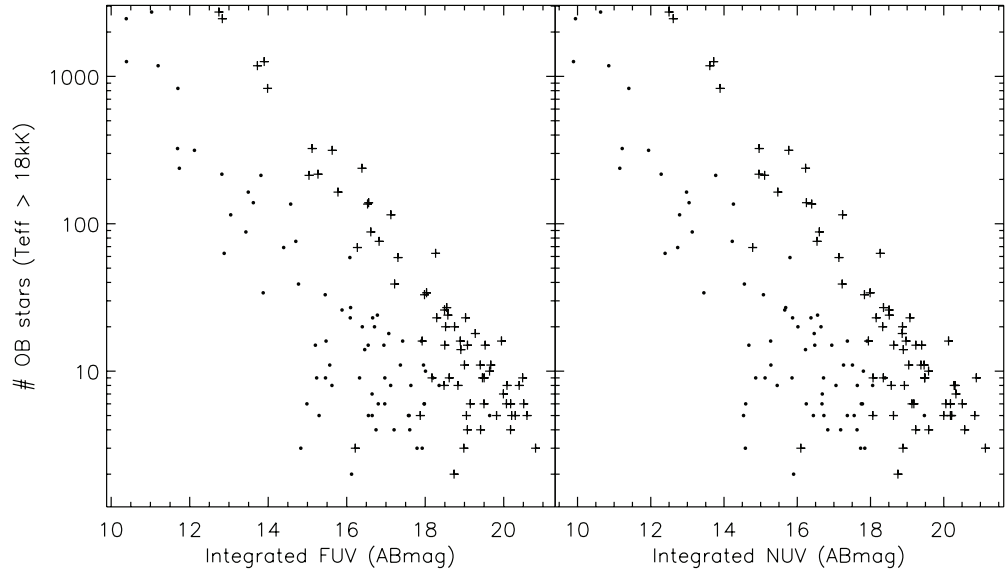

Figure 13. Integrated far-UV and near-UV fluxes of *GALEX*-defined star-forming regions (Kang et al. 2009) are compared with their hot-star content (number of *HST*-selected hot stars within each *GALEX*-region contour). Plus symbols are fluxes not dereddened; dots are *GALEX* fluxes dereddened with the average $E(B-V)$ of the hot stars they contain.

Table 4
Broadband Reddening Coefficient for Different Extinction Curves

	Type of Selective Extinction[a]			
	MW $R_V = 3.1$	LMCavg	LMC 2	SMC
$A_{F170W}/E(B-V)$	7.94	8.13	8.30	10.82
$A_{F255W}/E(B-V)$	6.69	6.11	5.86	6.85
$A_{F336W}/E(B-V)$	5.00	4.32	4.42	5.04
$A_{F439W}/E(B-V)$	4.11	3.34	3.54	3.93
$A_{F555W}/E(B-V)$	3.19	2.45	2.65	3.04
$A_{F814W}/E(B-V)$	1.88	1.25	1.39	1.68
E(F336W−F439W)/E(F439W−F555W)	0.96	1.10	0.98	1.25
E(F439W−F555W)/E(F555W−F814W)	0.71	0.74	0.71	0.66
E(F336W−F439W)/$E(B-V)$	0.89	0.97	0.88	1.11
E(F555W−F814W)/$E(B-V)$	1.31	1.20	1.25	1.36

Note. [a] The coefficients are derived from broadband model magnitudes, computed in the WFPC2 filters, after progressively reddening the model spectra over a range in $E(B-V)$ of 0–0.4 mag, and taking the average within the $T_{\rm eff}$ range 30,000–12,500 K. The four selective extinction curves are shown in Figure 3.

inside each *GALEX* contour, from this program, is about three times larger on average than hot-star counts obtained from the LGGS ground-based survey, within the same contours, due to the higher resolution of *HST* (many hot stars are in crowded regions, and are not resolved in ground-based data) and deeper photometry. Figure 13 shows a good overall correlation between the integrated far-UV flux and the number of hot stars; the scatter may be due to a small age range (our hot-star selection includes early-B stars, but the fraction of far-UV flux from O stars is much higher and the total flux will depend on the most massive stars still unevolved), possibly on the escape fraction, and certainly on the type of dust extinction (see Table 4 and Figure 3).

6. DISCUSSION AND SUMMARY

Our study provided a census of the hottest stars in 22 star-forming regions in M31, characterizing their massive star content, age of the populations, and the interstellar extinction. It also provides a six-band photometric catalog from 30 *HST* fields, complete to ∼23 mag in B and V and including over 10^5 massive stars. The fields span from 5.9 to about 22 kpc in deprojected galactocentric distance, with two fields in the north and south portions of the inner spiral arms (field 55 = OB10, and field 53 = OB22), many fields along or close to the "10 kpc star formation ring," the most conspicuous UV-bright galaxy-wide structure, four fields (two north and two south) on the next outer arm, and two outermost fields (NE and SW) on the faintest but still visible (in the *GALEX* UV imaging) spiral structure.

The choice of six-band photometry from far-UV to I yields particular leverage to discern the hottest stars, providing better sensitivity than other catalogs to ages of the order of a few to a few tens of millions of years. For about 15% of the total source catalog we have good photometry in enough filters to perform an SED analysis with model atmosphere colors, and derive $T_{\rm eff}$ and $E(B-V)$, although for a fraction of sources (crowded regions) photometry in UV filters seems too bright, causing $T_{\rm eff}$ to be overestimated. Tests with different model grids suggest that supersolar metallicity gives better fits for part of the sample, although the results also depend on the assumed type of selective extinction curve $A_\lambda/E(B-V)$. In some cases

UV-steep extinction curves produce better fits. In NGC 206 (OB78), covered with two contiguous *HST* fields, we measure about 7000 stars per field, similar to other fields in bright spiral arm portions, but there are three to four times more stars with small photometric errors, and hot stars, than in other fields with similar total source density (Table 3). The only other field that has a similarly high number of hot stars is OB54. The latter has an average $E(B-V) \sim 0.45$ mag, versus ~0.20 mag in NGC 206, making it presumably even richer intrinsically, since the observational limit is the same for all fields. Note that two fields were used to cover OB78, and one for OB54; therefore we are comparing here the number of stars per field. In total, OB78 is about twice as large and has about twice the number of hot stars, but less reddening.

Extinction, derived from individual stars with sufficient measurements in each region, has average values between $E(B-V) = 0.23$ and 0.33 mag for most regions, and up to $E(B-V) = 0.5$–0.6 mag (OB59, $E(B-V) = 0.57$ mag, OB66, $E(B-V) = 0.44$ mag). The outermost southwest field OB184 (22 kpc from the center) has an average of $E(B-V) = 0.12$ mag but OB157 (21 kpc, NE) has an average of $E(B-V) \sim 0.29$ mag. All derived values (Table 3) are higher than the foreground reddening derived by Schlegel et al. (1998), $E(B-V) = 0.06$ mag in the direction of M31. Such high extinction values from hot stars in general were also found by Kang et al. (2009). A relatively small average extinction, $E(B-V) = 0.20$ mag, is found in NGC 206 (OB78), the brightest and richest young complex in M31, suggesting that this region might be located higher above the disk than others in our sample. However, in a large spiral galaxy the actual dust distribution, confined overall to a thin equatorial disk (see, e.g., Figure 2 (bottom) of Bianchi et al. 2011a) is more clumpy than smooth, when looked at in detail, and this low extinction could also be a local effect, related to the intense starburst that blew away gas and dust from its surroundings (see, e.g., Figure 3 of Bianchi 2011). The west central fields have the highest reddening, significantly higher (by 0.1–0.2 mag) than the east-side fields. If an extinction curve steeper in UV than the adopted one were to be found appropriate in the star-forming regions, which can only be assessed with spectroscopic follow-up, the resulting $E(B-V)$ values would be smaller. Therefore, in general, the values from MW-type $A_\lambda/E(B-V)$ can be considered an upper limit, to be revised downward if a UV-steeper selective reddening were more appropriate. We also note that model colors for the hottest stars are not as blue as measured in real stars, and the results for the highest $T_{\rm eff}$ are necessarily more uncertain than for later types (e.g., Bianchi et al. 2012). This will be further investigated in a future work with follow-up spectroscopy. An overestimate of $T_{\rm eff}$ at the hottest end of the range would not affect our stellar counts and clustering properties (a $T_{\rm eff} > 18{,}000$ K limit was used). Derived values of $E(B-V)$ are provided in Table 3. They are plotted in Figure 14 with deprojected galactocentric distance, but given the sparse distribution of our pointings, the only obvious feature is an increase around the main star-forming structure (the "10 kpc ring"). A few sightlines in M31 were probed with UV spectroscopy by Bianchi et al. (1996), who found curves with similar slope to the MW general curve; more sightlines will be explored in *HST*'s cycle 19. Although our imaging probed distinct, individually selected regions, a peak is evident near the 10 kpc "ring" of star formation, as also found in the dust attenuation distribution estimated by Montalto et al. (2009) from UV-IR mapping of the whole disk. Tabatabaei & Berkhuijsen

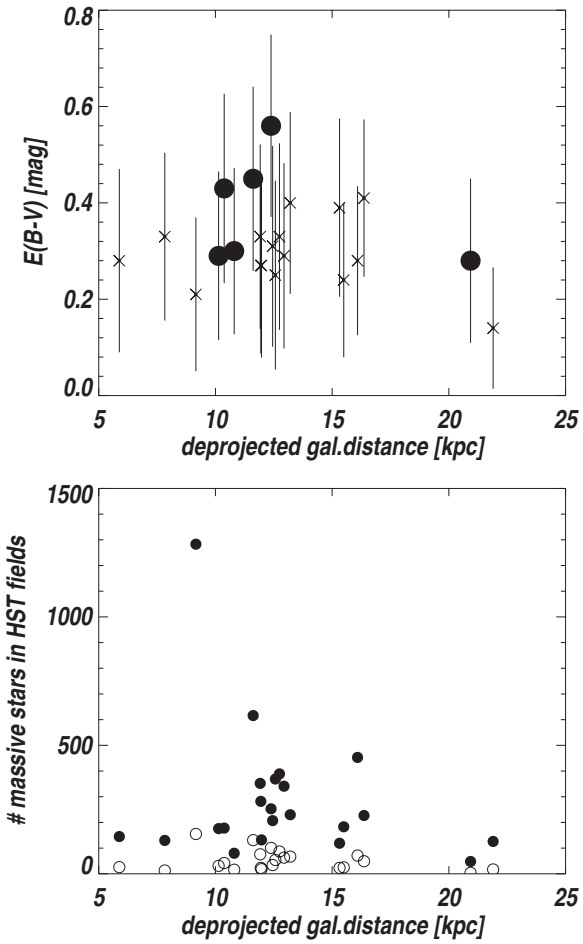

Figure 14. Average $E(B-V)$ in each region from Section 4 with deprojected distance (top): the filled dots mark regions OB157, OB54, OB59, OB69, OB66, and OB137. The bottom plot shows, for each region, the number of stars more massive than ~20 (circles) and 9 $M_\odot$ (dots) (see Section 6 for a discussion, and Section 4.3 for detailed discussion of the caveats, and uncertainties, as well as Table 4).

(2010) also noted a clear correlation of the dust temperature with the ring of enhanced star formation, stressing the coevolution of dust and star formation.

The bottom panel of Figure 14 is a related diagram, with plots of the numbers of stars more massive than 20 $M_\odot$ and 9 $M_\odot$ as a function of galactocentric distance. The numbers per field of the higher mass stars show a fairly level value between a few and ~150 stars, indicating the presence of significant recent activity over the entire range of galactocentric distances. The less massive stars, on the other hand, show a wide distribution of values, ranging from ~100 to ~1300. The highest number is for OB78 (NGC 206), the most luminous star-forming complex in M31.

We have explored spatial clustering of the hot stars on various scales, defining associations with sizes from a few parsecs across to ~100 pc. The density of hot stars in the associations varies with the parameters chosen for defining them with the clustering algorithm, especially the link-distance. While a by-eye delineation of associations (by a well trained eye) benefits from human wisdom being adaptable to each field conditions, our clustering algorithm allows us to explore in an objective way, with a homogeneous parameter choice, how the results vary in different fields, and to produce several catalogs of associations varying the definition criteria, to gather

statistical results. Comparison with UV-defined contours from low-resolution, deep *GALEX* far-UV maps, proved that the *GALEX* sensitivity did not miss any presence of hot stars, even sparse. The spatial scale to match the *GALEX*-defined contours of star-forming regions (at the threshold of 26 AB mag arcsec^{-2} in far-UV, used by Kang et al. 2009), implies a link-distance of 6 arcsec or more (depending on the region) from our *HST*-selected hot stars. Our quantitative definition of OB associations shows that the large, sparse regions (defined by a larger link-distance) of star formation are always composed of several more compact substructures, when looked at in detail. Such hierarchical structuring of star formation, long postulated, could be now quantified with *HST*-resolved studies of individual stars, by defining associations from single hot-star counts, probing different physical scales.

The cumulative mass distribution of the OB associations, derived by massive-star counts extrapolated with an IMF, roughly follows a power law, similar to what is found for the compact clusters, and H II regions (Hodge 1986a, 1986b). Studies of stellar clusters in the MW, Magellanic Clouds, and nearby galaxies, mostly concur that the cluster mass function follows one (or more) power law(s), and it can be described as $dN/dM_{\rm cl} \approx M_{\rm cl}{}^{\beta}$. Fairly consistent values have been found for β, of about -2 (e.g., Zhang & Fall 1999, for clusters in the 10^4–10^6 $M_\odot$ mass range in the Antennae; Lada & Lada 2003, for clusters in the 50–1000 $M_\odot$ range, in the solar neighborhood). Such slope is quite adequate also for representing the mass distribution of the OB associations (Figure 12, right); however, there is also an indication that the slope depends on the spatial scale (more or less compact) probed. A power-law distribution has also been found for the mass spectrum of molecular clouds, with typical β values around -1.6 (e.g., Muller et al. 2008; Blitz et al. 2007). Available spatial resolution of molecular and atomic gas maps is at best comparable to the *GALEX* resolution (>10–20 pc in M31); therefore resolution effects may also bias comparison among multi-wavelength results. The total hot-star count in our OB associations translates into a total stellar mass of $\gtrsim$0.6–0.8 $\times$ 10^6 $M_\odot$ recently formed in our sampled fields, by extrapolating the hot-star counts with a Kroupa (2001) IMF. Several caveats must be kept in mind: this number strongly depends on the assumed type of selective extinction (which could be constrained by follow-up spectroscopy), and analysis, as discussed in previous sections and exemplified in Table 4; we assumed a constant completeness limit of the hot-star counts (when estimated reddening is accounted for) in all fields, but again this depends on the reddening results; uncertainties in the hot-star counts derive from the presence of populations with a range of young ages, and from our $T_{\rm eff}$ values, which are possibly overestimated for a fraction of the sources; we assumed a constant mass range when extrapolating the hot-star counts to derive the total mass, but the upper mass limit may vary (this has a small effect on the total mass); the hot-star counts may be underestimated due to unresolved binaries. In addition, our fields selectively targeted star-forming regions, and are not representative of the average star formation density across the disk, but rather of the most active environments.

While our present *HST* program targeted the most conspicuous star-forming regions, and therefore only represent conditions favorable to intense star formation, the PHAT program (Dalcanton et al. 2012) will map with *HST* a large portion of the M31 disk, with deeper photometry in the optical and IR bands, plus one UV filter (WFC3/UVIS F275W), eventually enabling a comparison with the sparse interarm regions. Preliminary results (L. Bianchi et al. 2012, in preparation) suggest environmental differences in the properties of the OB associations, but a meaningful comparison can be performed only when enough area coverage will become available from the PHAT survey (OB associations are rare in the interarm regions). Our present catalog provides complementary information with more insight on the hottest (bright) stars in UV filters, to be compared with the deeper (and extended to redder objects and lower main sequence masses) CMDs from PHAT, in selected regions.

In future work, combining follow-up spectroscopy of selected subsamples, we hope to improve the extinction estimates, and to address the dynamical evolution of the associations, as well as explore the connection of the presently studied complexes to the more compact stellar clusters, on one hand, and with atomic and molecular gas on the other hand (see Hodge et al. 2010, 2011; P. W. Hodge et al. 2012, in preparation).

Support for program HST-GO-11079 was provided by NASA through a grant from the Space Telescope Science Institute, which is operated by the Association of Universities for Research in Astronomy, Inc., under NASA contract NAS 5-26555. We thank P. Massey and K. Olsen for many initial discussions in this program. The data were downloaded from the MAST archive.

Facility: HST (WFPC2)

REFERENCES

Aller, L. H., Appenzeller, I., Baschek, B., et al. 1982, Landolt-Bornstein: Numerical Data and Functional Relationships in Science and Technology, Vol. 2 (New York: Springer)
Barmby, P., Ashby, M. L. N., Bianchi, L., et al. 2006, ApJ, 650, L45
Barmby, P., Ashby, M. L. N., Bianchi, L., et al. 2007, ApJ, 655, L61
Barmby, P., & Huchra, J. 2001, AJ, 122, 2458
Bastian, N., Ercolano, B., & Gieles, M. 2009, Ap&SS, 324, 293
Bastian, N., Weisz, D. R., Skillman, E. D., et al. 2011, MNRAS, 412, 1539
Bernard, E., Ferguson, A. M. N., Barker, M. K., et al. 2012, MNRAS, 420, 2625
Bianchi, L. 2007, in UV Astronomy: Stars from Birth to Death, ed. A. I. Gomez de Castro & M. A. Barstow (Madrid: UCM Editorial Complutense), 65
Bianchi, L. 2009, Ap&SS, 320, 11
Bianchi, L. 2011, Ap&SS, 335, 51
Bianchi, L., Bohlin, R. C., & Massey, P. 2004, ApJ, 601, 228
Bianchi, L., Catanzaro, G., Scuderi, S., & Hutchings, J. B. 2001a, PASP, 113, 697
Bianchi, L., Clayton, G. C., Bohlin, R. C., Hutchings, J. B., & Massey, P. 1996, ApJ, 471, 203
Bianchi, L., & Efremova, B. V. 2006, AJ, 132, 378
Bianchi, L., Efremova, B., Herald, J., et al. 2011a, MNRAS, 411, 2770
Bianchi, L., Efremova, B., Hodge, P., et al. 2012, AJ, 143, 74
Bianchi, L., & Garcia, M. 2002, ApJ, 581, 610
Bianchi, L., Herald, J., Efremova, B., et al. 2011b, Ap&SS, 335, 161
Bianchi, L., Herald, J., & Garcia, M. 2009, in AIP Conf. Proc. 1135, Future Directions in Ultraviolet Spectroscopy, ed. Van Steenberg et al. (Melville, NY: AIP), 145
Bianchi, L., Kang, Y. B., Efremova, B., et al. 2011c, Ap&SS, 335, 249
Bianchi, L., Rodriguez-Merino, L., Viton, M., et al. 2007, ApJS, 173, 659
Bianchi, L., Scuderi, S., Massey, P., & Romaniello, M. 2001b, AJ, 121, 2020
Bianchi, L., Thilker, D. A., Burgarella, D., et al. 2005, ApJ, 619, L71
Blitz, L., Fukui, Y., Kawamura, A., et al. 2007, in Protostars and Planets V, ed. B. Reipurth, D. Jewitt, & K. Keil (Tucson, AZ: Univ. Arizona Press), 81
Bresolin, F., Kennicutt, R. C., Jr., Ferrarese, L., et al. 1998, AJ, 116, 119
Bresolin, F., Kudritzki, R.-P., Lennon, D. J., et al. 2002, ApJ, 580, 213
Brown, T. B., Sahu, K., Zoccali, M., et al. 2009, AJ, 137, 3172
Calzetti, D., Bohlin, R. C., Kinney, A. L., et al. 1995, ApJ, 443, 136
Calzetti, D., Kennicutt, R. C., Jr., Bianchi, L., et al. 2005, ApJ, 633, 871

Cardelli, J. A., Clayton, G. C., & Mathis, J. S. 1989, ApJ, 345, 245
Chapman, S. C., Ibata, R., Lewis, G. F., et al. 2006, ApJ, 653, 255
Corbelli, E., Lorenzoni, S., Walterbos, R., Braun, R., & Thilker, D. 2010, A&A, 511, 89
Cordiner, M. A., Cox, N. L. J., Evans, C. J., et al. 2011, ApJ, 726, 39
Coté, P., Mateo, M., Sargent, W., & Olsewzki, E. 2000, ApJ, 537, L91
Cuillandre, J.-C., Lequeux, J., Allen, R. J., Mellier, Y., & Bertin, E. 2001, ApJ, 554, 190
Dalcanton, J., et al. 2012, ApJS, 200, 18
de Vaucouleurs, G. 1958, ApJ, 128, 465
Dolphin, A. E. 2000, PASP, 112, 1383
Efremova, B. V., Bianchi, L., Thilker, D., et al. 2011, ApJ, 730, 88
Elmegreen, B. 2006, ApJ, 648, 572
Elmegreen, B. 2008, in ASP Conf. Ser. 388, Mass Loss from Stars and the Evolution of Stellar Clusters, ed. A. de Koter, L. J. Smith, & L. B. F. M. Waters (San Francisco, CA: ASP), 249
Garcia, M., & Bianchi, L. 2004, ApJ, 606, 497
Gil de Paz, Boissier, S., Madore, B. F., et al. 2007, ApJS, 173, 185
Girardi, L., Williams, B. F., Gilbert, K. M., et al. 2010, ApJ, 724, 1030
Gordon, K. D., Bailin, J., Engelbracht, C. W., et al. 2006, ApJ, 638, L87
Gordon, K. D., & Clayton, G. C. 1998, ApJ, 500, 816
Hodge, P. W. 1986a, in IAU Symp. 116, Luminous Stars and Associations in Galaxies, ed. C. W. H. De Loore et al. (Dordrecht: Reidel), 369
Hodge, P. W. 1986b, PASP, 98, 1095
Hodge, P. W. 1992, The Andromeda Galaxy (Astrophysics and Space Science Library, Vol. 176; Dordrecht: Kluwer)
Hodge, P. W., Krienke, O. K., & Bianchi, L. 2011, PASP, 123, 649
Hodge, P. W., Krienke, O. K., Bianchi, L., Massey, P., & Olsen, K. 2010, PASP, 122, 745
Johnson, L. C., et al. 2012, ApJ, 752, 95
Kang, Y. B., et al. 2012, ApJS, 199, 37
Kang, Y. B., Bianchi, L., & Rey, S.-C. 2009, ApJ, 703, 614
Krienke, O. K., & Hodge, P. 2007, PASP, 119, 7
Kroupa, P. 2001, MNRAS, 322, 231
Lada, C. J., & Lada, E. A. 2003, ARA&A, 41, 57
Lauer, T. R., Bender, R., Kormendy, J., Rosenfield, P., & Green, R. F. 2012, ApJ, 745, 121
Magnier, E. A., Battinelli, P., Lewin, W. H. G., et al. 1993, A&A, 278, 36
Marigo, P., Girardi, L., Bressan, A., et al. 2008, A&A, 482, 883
Marino, A., Bianchi, L., Rampazzo, R., et al. 2011, ApJ, 736, 154
Massey, P., Olsen, K. A. G., Hodge, P. W., et al. 2006, AJ, 131, 2478
Mathis, J. S. 1994, ApJ, 422, 176
McConnachie, A. W., Irwin, M. J., Ferguson, A. M. N., et al. 2005, MNRAS, 356, 979
McConnachie, A. W., Irwin, M. J., Ibata, R. A., et al. 2009, Nature, 461, 66
Misselt, K. A., Clayton, G. C., & Gordon, K. D. 1999, ApJ, 515, 128
Montalto, M., Seitz, S., Riffeser, A., et al. 2009, A&A, 507, 283
Morrissey, P., Conrow, T., Barlow, T. A., et al. 2007, ApJS, 173, 682
Mould, J., Saha, A., & Hughes, S. 2004, ApJS, 154, 623
Muller, S., Guelin, M., Ungerechts, H., et al. 2008, in Proc. Astrophysics and Space Science 2008, Mapping the Galaxy and Nearby Galaxies, ed. K. Wada & F. Combes (Berlin: Springer), 200
Pellerin, A., Fullerton, A. W., Robert, C., et al. 2002, ApJS, 143, 159
Rich, R. M., & Mighell, K. J. 1995, ApJ, 439, 145
Schlegel, D. J., Finkbeiner, D. P., & Davis, M. 1998, ApJ, 500, 525
Tabatabaei, F. S., & Berkhuijsen, E. M. 2010, A&A, 517, 77
Tanaka, M., Chiba, M., Komiyama, Y., et al. 2010, ApJ, 708, 1168
Thilker, D., Bianchi, L., Meurer, G., et al. 2007a, ApJS, 173, 538
Thilker, D., Boissier, S., Bianchi, L., et al. 2007b, ApJS, 173, 572
Thilker, D., Donovan, J., Schiminovich, D., et al. 2009, Nature, 457, 990
Thilker, D., Hoopes, C. G., Bianchi, L., et al. 2005, ApJ, 619, L67
Tolstoy, E., Hill, V., & Tosi, M. 2009, ARA&A, 47, 371
Trundle, C., Dufton, P. L., Lennon, D. J., Smartt, S. J., & Urbaneja, M. 2002, A&A, 395, 519
van den Bergh, S. 1964, ApJS, 9, 65
van den Bergh, S. 2000, The Galaxies of the Local Group (Cambridge Astrophysics Series, Vol. 35; Cambridge: Cambridge Univ. Press)
Walborn, N. R., Fullerton, A. W., Crowther, P. A., et al. 2002, ApJS, 141, 443
Wray, J., & de Vaucouleurs, G. 1980, AJ, 85, 1
Zhang, Q., & Fall, S. M. 1999, ApJ, 527, L81